Biophysical models reveal the relative importance of transporter proteins and impermeant anions in chloride homeostasis

Kira M. Düsterwald[1], Christopher B. Currin[*1], Richard J. Burman[*1], Colin J. Akerman[2], Alan R. Kay[3], Joseph V. Raimondo[1]

[*]Authors contributed equally

[1]Division of Cell Biology, Department of Human Biology, Neuroscience Institute and Institute of Infectious Disease and Molecular Medicine, Faculty of Health Sciences, University of Cape Town, Cape Town, South Africa

[2]Department of Pharmacology, University of Oxford, Oxford, United Kingdom

[3]Department of Biology, University of Iowa, Iowa City Iowa, USA

Correspondence:
Joseph V. Raimondo
email: joseph.raimondo@uct.ac.za

and

Alan R. Kay
email: alan-kay@uiowa.edu

Running Title
The cellular determinants of Cl^- driving force in the nervous system.

Impact statement
Impermeant anions may influence chloride concentration in neurons, but do not appreciably change chloride driving force, the parameter important for inhibitory signaling.

Keywords
Chloride, cation-chloride cotransport, impermeant anions, KCC2, Na^+/K^+ ATPase, inhibition, GABA

Acknowledgements
We would like to thank Juha Voipio for critically reading the manuscript and providing helpful comments and suggestions.

Abstract

Fast synaptic inhibition in the nervous system depends on the transmembrane flux of Cl^- ions based on the neuronal Cl^- driving force. Established theories regarding the determinants of Cl^- driving force have recently been questioned. Here we present biophysical models of Cl^- homeostasis using the pump-leak model. Using numerical and novel analytic solutions, we demonstrate that the Na^+/K^+-ATPase, ion conductances, impermeant anions, electrodiffusion, water fluxes and cation-chloride cotransporters (CCCs) play roles in setting the Cl^- driving force. Our models, together with experimental validation, show that while impermeant anions can contribute to setting $[Cl^-]_i$ in neurons, they have a negligible effect on the driving force for Cl^- locally and cell-wide. In contrast, we demonstrate that CCCs are well-suited for modulating Cl^- driving force and hence inhibitory signalling in neurons. Our findings reconcile recent experimental findings and provide a framework for understanding the interplay of different chloride regulatory processes in neurons.

53 *Introduction*

54 Fast synaptic inhibition in the nervous system is mediated by type A γ-aminobutyric acid receptors
55 ($GABA_ARs$) and glycine receptors (GlyRs), which are primarily permeable to chloride (Cl^-) (Farrant and
56 Kaila, 2007). Together with the neuronal membrane potential, the transmembrane gradient for Cl^-
57 sets the driving force for Cl^- flux across these receptors, controlling the properties of inhibitory
58 signaling. Modification of neuronal intracellular Cl^- concentration ($[Cl^-]_i$) has been shown to play a
59 causative role in multiple neurological diseases including epilepsy, chronic pain, schizophrenia and
60 autism (Rivera et al., 2004; Huberfeld et al., 2007; Price et al., 2009; Hyde et al., 2011; Tyzio et al.,
61 2014). Similarly, intracellular Cl^- is thought to be modulated during brain development so that
62 GABAergic transmission contributes optimally to the construction of neural circuits (Ben-Ari, 2002).
63 Given the importance of Cl^- for brain function and dysfunction, the cellular mechanisms that control
64 its transmembrane gradient and driving force are of considerable interest.

65

66 Plasmalemmal Cl^- transporters, in particular cation-chloride cotransporters (CCCs), are understood to
67 be the major mechanism by which neurons regulate the driving force for Cl^- permeable anion channels
68 (Kaila et al., 2014). Recently, it has been suggested that in fact impermeant anions control local $[Cl^-]_i$
69 and driving force (Glykys et al., 2014), rather than the CCCs. The majority of intracellular anions are
70 impermeant to the neuronal membrane; these include ribo- and deoxynucleotides, intracellular
71 proteins and metabolites (Burton, 1983). Impermeant anions induce what is known as the Donnan (or
72 Gibbs-Donnan) effect (Hill, 1956; Sperelakis, 2012) – an uneven distribution of impermeant molecules
73 across the membrane which is osmotically unstable. Without active ion transport to counter this
74 effect, neurons would swell and burst (Kay, 2017). Animal cells, including neurons, maintain cell
75 volume in the presence of impermeant anions by using the Na^+/K^+-ATPase to pump Na^+ out of the cell
76 and K^+ in, along with the passive movement of water and other ions (Tosteson and Hoffman, 1960;
77 Armstrong, 2003; Liang et al., 2007; Kay, 2017). This pump-leak mechanism, whilst stabilizing cell
78 volume, also establishes the negative resting membrane potential and transmembrane Na^+ and K^+

79 gradients, which serve as energy sources for the coupled transport of other molecules, including Cl^-
80 by CCCs. In the absence of active Cl^- transport, $[Cl^-]_i$ is set by the membrane potential; i.e. the Nernst
81 potential of Cl^- ($E_{Cl} = \frac{RT}{F} \ln \frac{Cl_i}{Cl_o}$) equals the transmembrane potential (V_m).
82
83 The transmembrane Cl^- gradient and the driving force ($DF=V_m-E_{Cl}$) for Cl^- permeable ion channels are
84 therefore the outcome of multiple, dynamically interacting mechanisms. This makes experimental
85 investigation of the determinants of Cl^- driving force difficult, particularly at a local level.
86 Computational models based on established biophysical first principles are productive means for
87 exploring the roles of cellular mechanisms in generating local Cl^- driving force. Here, we establish
88 numerical and novel analytic solutions for an inclusive model of Cl^- homeostasis to elucidate the
89 determinants of the neuronal driving force for Cl^-.
90
91 We demonstrate that baseline $[Cl^-]_i$ is a product of the interaction of Na^+/K^+-ATPase activity, the
92 average charge of impermeant anions, ion conductances, CCCs and water permeability. Consistent
93 with recent experimental reports (Glykys et al., 2014), and our own experimental validation using
94 electroporation of anionic dextrans and optogenetic probing of E_{GABA}, we find that impermeant anions
95 can contribute to setting $[Cl^-]_i$. However, we find that they can only affect the Cl^- driving force by
96 modifying active transport mechanisms, and then only negligibly. Impermeant anions therefore do
97 not appreciably modify synaptic signaling properties, contrary to recent experimental interpretation
98 (Glykys et al., 2014). In contrast, we demonstrate using biophysical models and gramicidin perforated-
99 patch clamp recordings that CCCs selectively regulate substantial changes in the Cl^- driving force. This
100 is consistent with a meta-analysis of experimental data from the field, which shows a strong
101 correlation between the activity of the specific CCC, KCC2, and Cl^- driving force. The ability of CCCs to
102 specifically modulate Cl^- at a local level depends on the characteristics of Cl^- electrodiffusion in the
103 structure concerned, demonstrated using multicompartment modelling. Together, our models

provide a theoretical framework for understanding the interplay of chloride regulatory processes in neurons and interpreting experimental findings.

106 *Results*

107 A biophysical model based on the pump-leak mechanism demonstrates the importance of the sodium-
108 potassium ATPase for setting transmembrane ion gradients including chloride.

109 To compare the effects of impermeant anions and Cl^- cotransport on Cl^- homeostasis we first
110 developed a single compartment model based on the pump-leak formulation (Tosteson and Hoffman,
111 1960; Kay, 2017) (**Fig. 1A**). This model, defined by a set of differential equations, incorporated
112 mathematical representations of the three major permeable ion species Cl^-, K^+, Na^+ as well as
113 impermeant anions (X^z) with average charge z. Permeable ions could move across the cellular
114 membrane via passive conductances according to each ion's respective electrochemical gradient.
115 Further, active transport of Na^+ and K^+ by the Na^+/K^+-ATPase and cotransport of Cl^- and K^+ by the
116 cation-chloride cotransporter KCC2 with a non-zero conductance g_{KCC2} of 20 µS/cm^2 unless otherwise
117 stated were included. Finally, our formulation accounted for the dynamics of cell volume (w),
118 intracellular osmolarity (Π) and transmembrane voltage (V_m) (see Materials and Methods).
119 Importantly, regardless of initial starting concentrations of permeant or impermeant ions, cell volume
120 or V_m, the model converged to stable fixed points without needing to include any means for 'sensing'
121 ion concentration, volume or voltage. In the case of permeable ions, initial concentrations did not
122 even determine the final cellular volume. For example, despite initiating the model with different
123 starting concentrations of Cl^- (1, 15, 40 and 60 mM respectively, **Fig. 1B**), the $[Cl^-]_i$ always converged
124 to the same stable concentration of 5.2 mM, a typical baseline $[Cl^-]_i$ for adult neurons, and volume
125 always converged to 2.0 pL, a typical volume for hippocampal neurons (Ambros-Ingerson and Holmes,
126 2005). The model is robust in the sense that its convergence to a stable steady state does not depend
127 on a narrow set of parameters and initial values. Another proposed model of the Na^+/K^+-ATPase with
128 experimental validation (Hamada et al., 2003) parameterized for our steady state values had similar
129 activity in terms of net flux rate in our range of $[Na^+]_i$ and invariance to initial permeable ionic
130 concentrations, (**Figure 1 – figure supplement 1A-B**).

131

132 Consistent with previous results (Xiao et al., 2002; Dierkes et al., 2006; Dijkstra et al., 2016), 'turning
133 off' the activity of the Na^+/K^+-ATPase in our model led to a progressive collapse of transmembrane ion
134 gradients, progressive membrane depolarization and continuous and unstable cell swelling. Such
135 effects could be reversed by reactivation of the pump (**Fig. 1C**). The relative activity of the Na^+/K^+-
136 ATPase sets the final stable values for ion concentrations (of both permeable and impermeant ions),
137 V_m and volume (**Fig. 1C**). When we increased the activity of the Na^+/K^+-ATPase in our model, the final
138 steady-state concentration for K^+ increased, whilst Na^+ and Cl^- dropped to levels that approximate
139 those observed in mature neurons (**Fig. 1D**). At the same time, the final, stable-state membrane
140 potential and cell volume also decreased. Interestingly, as has been observed previously (Fraser and
141 Huang, 2004), beyond a certain level, further increases in Na^+/K^+-ATPase activity have negligible
142 effects on cell volume and transmembrane voltage. For subsequent analysis, we chose a 'default'
143 effective pump rate for the Na^+/K^+-ATPase of approximately 1.0×10^{-2} C/(dm^2.s), that is a pump rate
144 constant of 10^{-1} C/(dm^2.s) (equation (2)), and average intracellular impermeant anion charge (z) of -
145 0.85 as extrapolated from reasonable cellular ionic concentrations and osmolarity (Lodish et al., 2009;
146 Raimondo et al., 2015). This resulted in steady-state ion concentrations and membrane potentials that
147 approximate those experimentally observed in mature neurons: Cl^- 5 mM; K^+ 123 mM; Na^+ 14 mM; X^z
148 155 mM; and a V_m of -72.6 mV (Jiang and Haddad, 1991; Diarra et al., 2001; Tyzio et al., 2008). We
149 were able to corroborate the numerical solutions for final steady-state values by developing a
150 parametric-analytic solution (**Supplementary file 1**). We observed exact correspondence between the
151 numerical and analytic solutions within our model (**Fig. 1D**). In subsequent analyses, this novel analytic
152 solution allowed us to explore rapidly a large parameter space to determine how various cellular
153 attributes might affect Cl^- homeostasis.
154

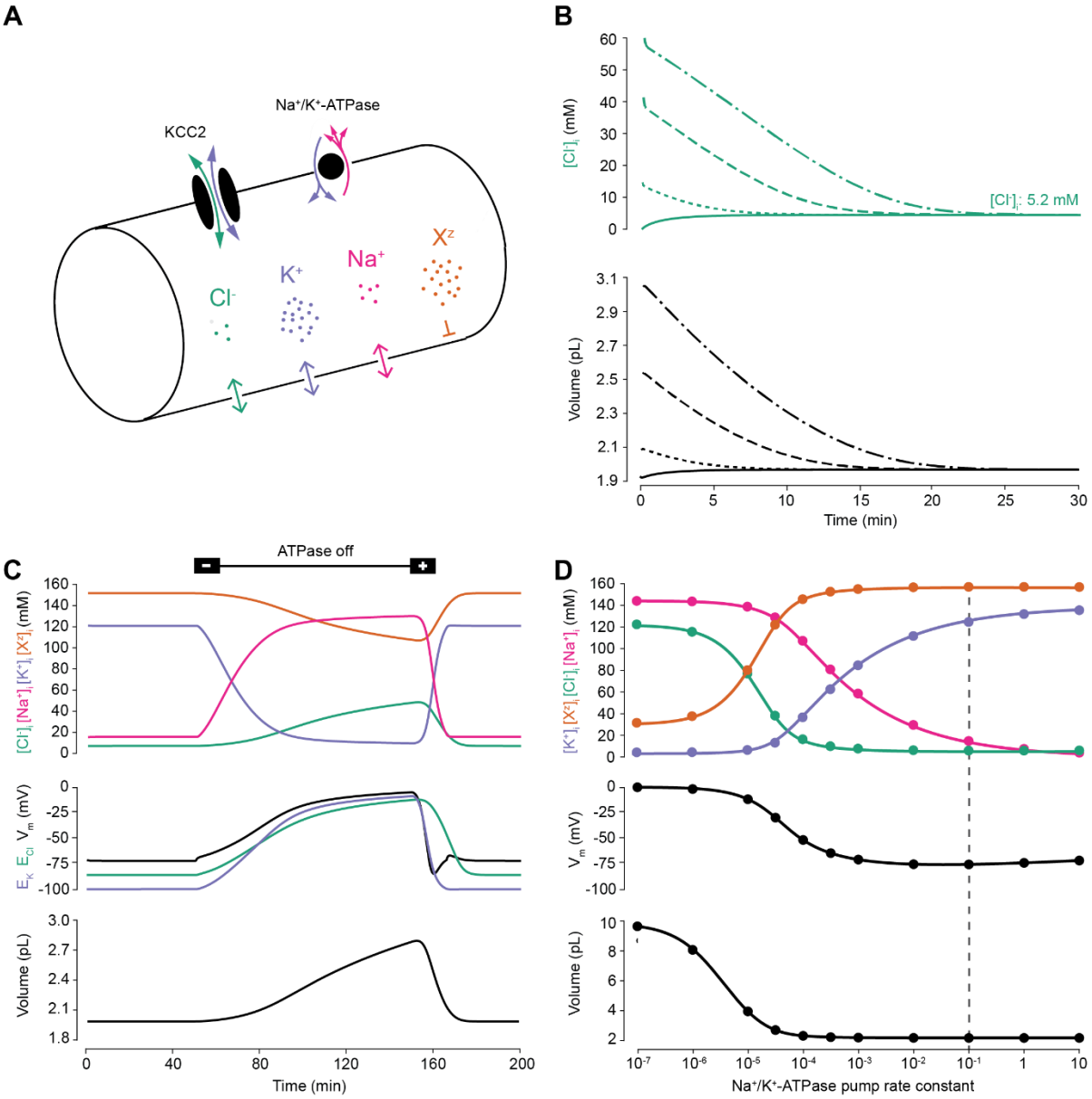

155

156 *Figure 1: A biophysical model of ion dynamics based on the pump-leak mechanism demonstrates the*

157 *importance of the sodium-potassium ATPase for setting transmembrane ion gradients including*

158 *chloride. (A) A single cell compartment was modelled as a cylinder with volume changes equivalent to*

159 *changes in cylindrical radius. Dynamics of membrane permeable potassium (purple, K^+), sodium (pink,*

160 *Na^+) and chloride (green, Cl^-) ions were included. Impermeant anions (orange, X^z) had an average*

161 *intracellular charge z. The KCC2 transporter moved Cl^- and K^+ in equal parts according to the*

162 *transmembrane gradient for the two ions. The sodium-potassium ATPase transported 3 Na^+ ions out*

163 *for 2 K^+ ions moved into the cell. (B) Regardless of intracellular starting concentrations of the*

164 *permeable ions, the model converged to identical steady state values for all parameters without*

needing to include any means for 'sensing' ion concentration, volume or voltage. We show the result for Cl^- as a time series of $[Cl^-]_i$ (top panel) and volume (bottom panel). (C) The ATPase plays a key role in maintaining steady state ion concentration, membrane voltage (V_m) and volume. Switching off the ATPase results in a continuous increase in cell volume (bottom panel), membrane depolarization (middle panel) and ion concentration dysregulation (top panel with colours per ion as in 'A'. All cellular parameters recovered when the ATPase was reactivated. (D) The model's analytic solution showed exact correspondence with steady state values generated by numerical, time series runs (dots) for varying ATPase pump rates. Steady state values for the concentrations of the ions with colours as in A (top panel); V_m (middle panel) and volume (bottom panel). The dashed line indicates the default ATPase pump rate used in all simulations unless specified otherwise. The result in (B) is replicated with Hamada et al.'s experimentally validated model of the ATPase in Figure 1 – figure supplement 1B, and the models' respective pump fluxes are compared in figure supplement 1A.

<u>Membrane chloride conductance affects steady-state intracellular chloride concentration only in the presence of cation-chloride cotransport.</u>

Using the analytic solution, we investigated how changes in baseline ion conductance for the major ions in our model (g_K, g_{Na} and g_{Cl}) affected Cl^- homeostasis. We calculated the steady-state values for the Cl^- reversal potential (E_{Cl}) and potassium reversal potential (E_K), resting membrane potential (V_m) and volume (w) whilst independently manipulating the conductance for each ion (**Fig. 2**). Increasing the baseline potassium conductance (g_K) resulted in E_{Cl}, E_K and V_m converging to similar steady-state values (**Fig. 2A**) without significantly affecting cell volume. We were also able to replicate the classic dependence of membrane potential on $\log([K^+]_o)$ (**Figure 2 – figure supplement 1**). In contrast, increasing the baseline sodium conductance (g_{Na}) beyond 20 $\mu S/cm^2$ resulted in a steady depolarization of E_{Cl}, E_K and V_m with accompanying cell swelling (**Fig. 2B**).

190 The effect of manipulating Cl^- conductance (g_{Cl}) depended on the activity of concurrent cation-chloride
191 cotransport by KCC2 (**Fig. 2C**). In the presence of active KCC2 at very low values of g_{Cl}, the steady state
192 $[Cl^-]_i$ is such that E_{Cl} approaches E_K. This follows because in the absence of alternative Cl^- fluxes, KCC2
193 utilizes the transmembrane potassium gradient to transport Cl^- until E_{Cl} equals E_K. With increasing g_{Cl}
194 however, E_{Cl} increases, moving away from E_K towards V_m, and at very high Cl^- conductances E_{Cl} and V_m
195 approached similar values in our model. Without the activity of KCC2, g_{Cl} had no effect on steady state
196 E_{Cl}, E_K, V_m or volume, with g_{cl} able to be very low but greater than zero (**Fig. 2D**). In this instance E_{Cl}
197 always equals V_m as the movement of Cl^- across the membrane is purely passive. Without the activity
198 of KCC2, there can be no driving force for Cl^- flux at steady state (V_m-E_{Cl} = 0). Our model therefore
199 behaved in a manner consistent with established theoretical predictions (Kaila et al., 2014).
200

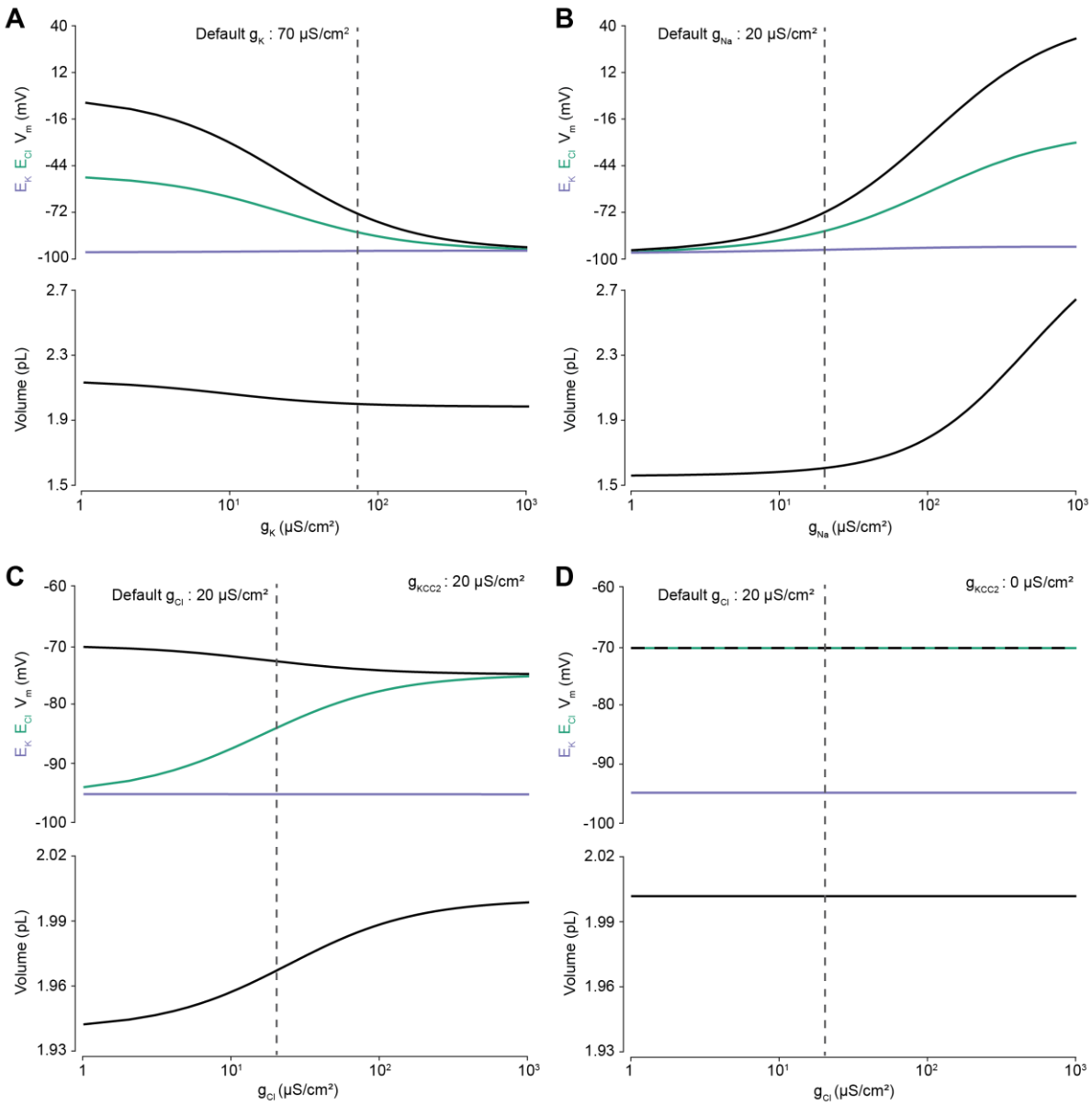

<u>Figure 2: Membrane chloride conductance affects steady-state intracellular chloride concentration only in the presence of cation-chloride cotransport.</u> Steady state values for different ionic conductance were calculated using the model's analytic solution. (A) Steady state E_{Cl} (green), E_K (purple), V_m (black) and volume w (bottom panel) were calculated at different K^+ conductances (g_K). Increasing g_K resulted in a convergence of steady state E_{Cl}, E_K and V_m. (B) Increasing Na^+ conductance g_{Na} resulted in a progressive increase in steady state E_{Cl}, E_K and V_m with accompanying cell swelling. (C) In the presence of active cation-chloride cotransport (g_{KCC2} = 20 µS/cm^2), increasing Cl^- conductance shifted steady state E_{Cl} from E_K toward V_m. (D) In the absence of KCC2 activity, g_{Cl} had no effect on steady state parameters. E_{Cl} equals V_m in all instances. Dashed lines indicate the default values for g_K, g_{Na} and g_{Cl}.

211 *In Figure 2 – figure supplement 1 the classic dependence of the membrane potential on log($[K^+]_o$) is*
212 *shown.*
213
214 Cation-chloride cotransport sets the chloride reversal and driving force for transmembrane chloride
215 flux.
216 Next, we used our single-cell unified model to explore how the activity of cation-chloride cotransport
217 affects Cl^- homeostasis. In our model, the activity of KCC2 is set by the conductance of KCC2 (g_{KCC2}).
218 Using the numerical formulation with the default values described in Figure 1 and 2, we steadily
219 increased g_{KCC2} from 20 µS/cm^2 to 370 µS/cm^2 and tracked changes to E_{Cl}, E_K, V_m and volume. Increasing
220 KCC2 activity over time caused a steady decrease in $[Cl^-]_i$ reflected by a hyperpolarization of E_{Cl} (**Fig.**
221 **3A**). V_m decreased only modestly, resulting in an increase in the driving force for Cl^- flux that tracks the
222 increase in g_{KCC2}. This effect saturates as E_K constitutes a lower bound on E_{Cl}. Importantly, increases in
223 g_{KCC2} resulted in persistent changes to E_{Cl} and the driving force for Cl^-. Employing alternate models for
224 KCC2 (Fraser and Huang, 2004; Lewin et al., 2012; Raimondo et al., 2012) and the ATPase (Hamada et
225 al., 2003) did not change this result when compensation for parameterization was given, although
226 different KCC2 models result in different kinetic rates for Cl^- and K^+ transport (**Figure 3 – figure**
227 **supplement 1 and 2**). Using the analytic solution to our model we calculated how KCC2 activity affects
228 steady state values of E_{Cl}, E_K, V_m, w and Cl^- driving force (**Fig. 3B**). In confirmation of our findings in
229 Figure 2D, with no KCC2 activity (g_{KCC2} = 0), E_{Cl} equaled V_m and the Cl^- driving force was zero. As we
230 increased g_{KCC2}, steady state E_{Cl} pulled away from V_m and approached E_K. This resulted in an increase
231 in Cl^- driving force (V_m-E_{Cl}) with steady state values of 11.3 mV at our chosen default value of g_{KCC2}. The
232 results obtained with our model are therefore fully consistent with the view that CCCs, in this case
233 KCC2, establish the driving force for Cl^-.
234
235 To test this theoretical finding, we performed gramicidin perforated patch-clamp recordings from CA3
236 hippocampal neurons in rat organotypic brain slices whilst activating Cl^- permeable $GABA_A$ receptors

237 with muscimol (10 µM), in order to measure the $GABA_AR$ driving force, which approximates Cl^- driving
238 force (**Fig. 3C**). We then tested our model predications by applying the CCC blocker, furosemide (1
239 mM) (**Fig. 3D, E**). We noted that after furosemide was introduced the E_{GABA} became significantly more
240 depolarized (baseline: -78.81 ± 2.78 mV vs furosemide: -71.59 ± 3.04 mV, *n* = 10, *p* = 0.01, *paired t-*
241 *test*) whilst there was no significant difference in V_m (-69.92 ± 1.77 mV vs -71.51 ± 2.61 mV, *n* = 10, *p*
242 = 0.36, *paired t-test*) (**Fig. 3E**). This reflects a significant change in the $GABA_AR$ driving force (8.89 ±
243 3.44 mV vs 0.08 ± 4.57 mV, *n* = 10, *p* = 0.04, *paired t-test*). Furthermore, we then noted that this
244 change in driving force persisted for at least 15 minutes post application of furosemide (**Fig. 3F**). These
245 results are consistent with our model predictions and demonstrate how the application of a CCC
246 blocker reduces the $GABA_AR$ driving force (and hence Cl^- driving force) by selectively depolarizing E_{GABA}
247 with negligible effects on V_m.
248
249 In addition, we sought experimental data from the literature to determine whether changes in KCC2
250 activity correlate with alterations to steady-state $[Cl^-]_i$. We focused on changes in KCC2 expression
251 level, as this is likely to be a strong predictor of changes in KCC2 activity. Indeed, in a meta-analysis of
252 7 studies and 8 experiments from our review of 26 studies, weighted for methodological biases and
253 data quality, we observed a significant correlation ($R^2 = 0.796$, $p < 0.001$) between the change in KCC2
254 expression and Cl^- driving force (**Fig. 3G**). Absolute changes in V_m were less than 2 mV in all but one
255 study, meaning that the change in driving force could be ascribed to significant shifts in E_{GABA} (R^2 =
256 0.045, $p < 0.001$). The outlier data point (showing a 8.45 mV change) was from a study into the effects
257 of acute stress, where other factors could have transiently influenced V_m (MacKenzie and Maguire,
258 2015). The meta-analysis supports the prediction that cation-chloride cotransport by KCC2 is an
259 important determinant of $[Cl^-]_i$ ($R^2 = 0.83$, $p < 0.001$, 9 studies) and driving force (see **Supplementary**
260 **file 2 Table S2-1** for raw data, and the scoring table for weighting in **Table S2-2**).
261

262 Since Cl^- cotransport by KCC2 depends on the transmembrane gradient for K^+, which in turn is
263 established by the Na^+/K^+-ATPase, we explored how the Na^+/K^+-ATPase pump rate affected E_{Cl} in the
264 presence of KCC2 activity (g_{KCC2} = 20 µS/cm^2). As depicted in **Fig. 3H**, the Na^+/K^+-ATPase pump is a
265 critical determinant of intracellular Cl^- homeostasis. Of interest, above a pump rate constant of 10^{-3}
266 C/(dm^2.s), where cell volume is stable, even many fold changes in pump rate have minimal effects on
267 E_{Cl} and V_m. It therefore seems unlikely that neurons would adjust the Na^+/K^+-ATPase to modulate Cl^-
268 driving force.

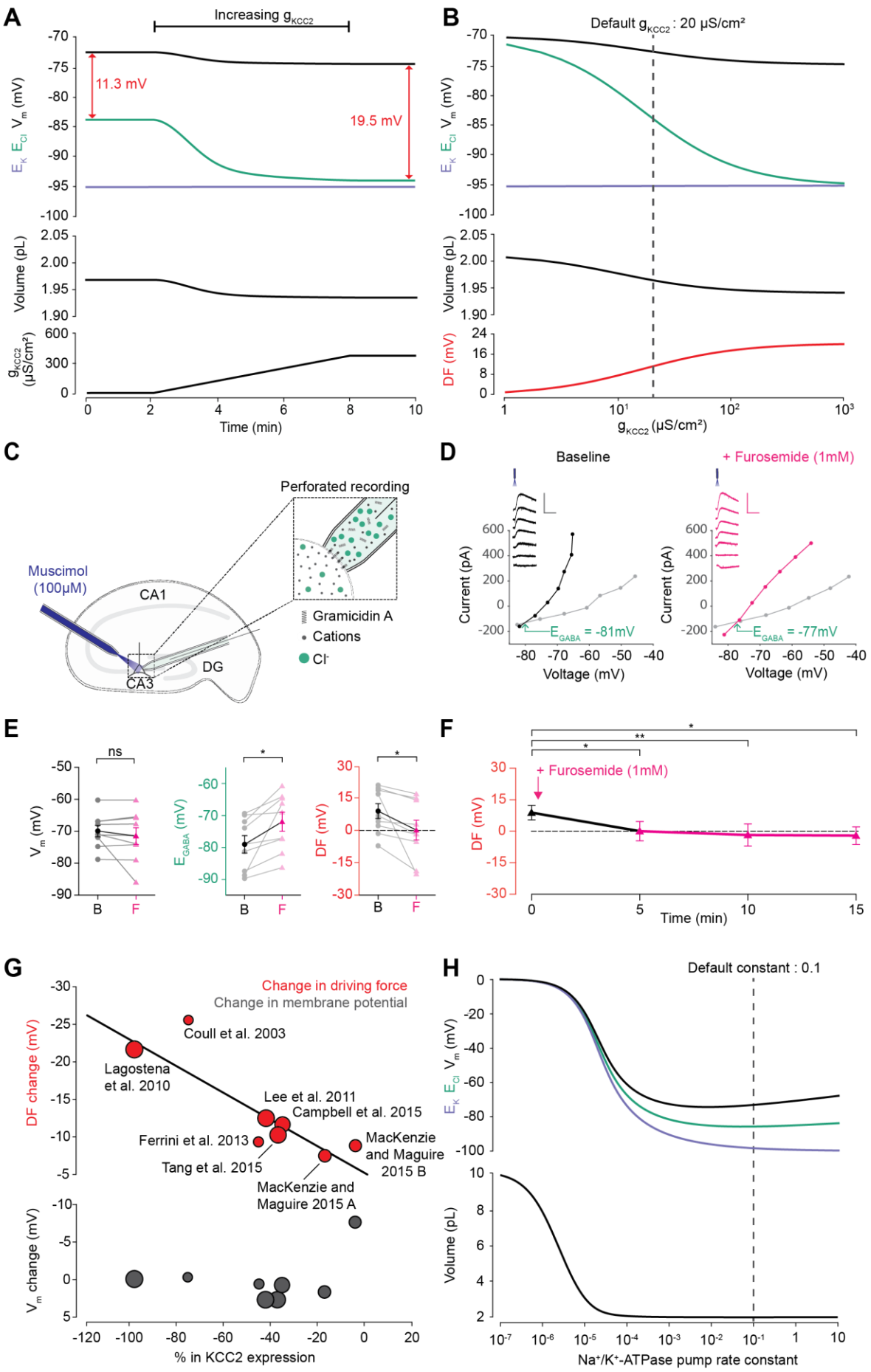
A
Increasing g_{KCC2}
11.3 mV
19.5 mV
E_K E_{Cl} V_m (mV)
Volume (pL)
g_{KCC2} (µS/cm²)
Time (min)
B
Default g_{KCC2} : 20 µS/cm²
DF (mV)
g_{KCC2} (µS/cm²)
C
Perforated recording
Muscimol (100µM)
CA1
CA3
DG
Gramicidin A
Cations
Cl⁻
D
Baseline
+ Furosemide (1mM)
Current (pA)
E_{GABA} = -81mV
E_{GABA} = -77mV
Voltage (mV)
E
ns
V_m (mV)
E_{GABA} (mV)
DF (mV)
B
F
F
+ Furosemide (1mM)
DF (mV)
Time (min)
G
Change in driving force
Change in membrane potential
DF change (mV)
Coull et al. 2003
Lagostena et al. 2010
Lee et al. 2011
Campbell et al. 2015
Ferrini et al. 2013
Tang et al. 2015
MacKenzie and Maguire 2015 B
MacKenzie and Maguire 2015 A
V_m change (mV)
% in KCC2 expression
H
Default constant : 0.1
E_K E_{Cl} V_m (mV)
Volume (pL)
Na⁺/K⁺-ATPase pump rate constant

269

270 *Figure 3: Cation-chloride cotransport sets the chloride reversal and driving force for transmembrane*
271 *chloride flux.* *(A) Increasing KCC2 activity in our model by increasing g_{KCC2} from 20 µS/cm^2 to 370 µS*
272 */cm^2 resulted in a persistent decrease in E_{Cl} (green), a minimal decrease in E_K (purple), V_m (black) and*
273 *volume w (bottom panel). This resulted in a permanent increase in the DF for Cl^- via a change in E_{Cl}*
274 *from -83.9 mV to -93.2 mV (red). (B) The steady state values for E_{Cl}, E_K, V_m (top panel), volume (middle*
275 *panel) and Cl^- driving force (DF, bottom panel, red) at different KCC2 conductances. Increasing KCC2*
276 *activity resulted in a decrease in steady state E_{Cl} and DF. E_K represented a lower bound on E_{Cl} at high*
277 *KCC2 conductances. Similar results were noted for other kinetic models of KCC2 (figure supplement 1*
278 *and 2). (C) Schematic showing experimental setup. Gramicidin perforated patch-clamp recordings*
279 *were performed on CA3 pyramidal cells from rat hippocampal organotypic brain slices. (D) Insets depict*
280 *$GABA_AR$ currents elicited by somatic application (20 ms) of muscimol (10 µM) at different voltages.*
281 *Calibration: 500 ms, 500 pA. Current-voltage (IV) plots with holding current (reflecting membrane*
282 *current, grey) and total current (reflecting membrane current plus the muscimol-evoked current, black*
283 *or pink) were drawn to calculate changes in V_m, E_{GABA} and DF before (left, black) and after (right, pink)*
284 *furosemide was applied. Voltages were corrected for series resistance error. (E) Population data*
285 *showing significant changes in E_{GABA} and DF but not V_m five minutes after furosemide application. (F)*
286 *Changes in DF over time show a significant decrease from baseline once furosemide was introduced.*
287 *(G) Meta-analysis of experimental studies demonstrates a correlation between KCC2 activity (%*
288 *change) and Cl^- DF (mV, top plot, red) but not membrane potential (mV, bottom plot, grey), confirming*
289 *the role of KCC2 for establishing the neuronal Cl^- gradient in adult tissue. The data and scoring system*
290 *used to generate the regression can be found in Supplementary file 2 (Tables S2-1 and S2-2). (H)*
291 *Sufficient Na^+/K^+-ATPase activity is critical for steady state ionic gradients, V_m (top panel, colours as in*
292 *'A') and volume (bottom panel), but these variables are relatively stable near the default pump rate*
293 *(dashed line). 'ns', non-significant; *p <0.05; ** p<0.01.*
294

295 Altering the concentration of intracellular or extracellular impermeant anions, without changing the
296 average charge of impermeant anions, does not affect the steady state gradient or driving force for
297 chloride.
298 To determine the effect of impermeant anions on Cl^- homeostasis we first explored whether adjusting
299 the concentration of impermeant anions ($[X]_i$), while maintaining a constant average impermeant
300 anion charge (z), had any impact on E_{Cl}, E_K, V_m or volume. We initiated the full single-compartment
301 model with different starting concentrations of impermeant anions (but the same average charge, z =
302 -0.85), and observed that regardless of the initial concentration of impermeant anions, over a period
303 of minutes, the cell adjusted its volume to give an identical steady-state impermeant anion
304 concentration (**Fig. 4A**, $[A]_i$ = 155 mM). Analytically, it can be shown that the number of moles of X
305 determines completely the volume of the compartment, while the permeant ions alone cannot be
306 used to predict steady state volume (Kay, 2017). Similarly, all initial impermeant anion concentrations
307 resulted in identical steady state values of E_{Cl} (-83.8 mV), E_K (-95.1 mV) and V_m (-72.6 mV) (**Fig. 4B**).
308 This shows that simply adjusting the amount of impermeant anions within a cell has no persistent
309 effect on $[Cl^-]_i$.
310
311 We then tested the effect of dynamically adding impermeant anions with the default average charge
312 either intracellularly (**Fig. 4C**) or extracellularly (**Fig. 4D**). While impermeant anions are being added to
313 the cell, the membrane potential hyperpolarizes and E_{Cl} decreases. However, following the cessation
314 of impermeant anion influx, E_{Cl}, E_K, V_m and $[X]_i$ return to steady state values due to compensatory
315 changes to cell volume (**Fig. 4C**). There are transient transmembrane fluxes of all ions while anions are
316 added into the cell, and in particular the inward flux of the cations Na^+ and K^+, such that the sum $[X]_i$
317 + $[Cl^-]_i$ is not necessarily kept constant during impermeant anion addition (**Figure 4 – figure**
318 **supplement 1**). Impermeant ions (with default average charge) were added to the extracellular space,
319 which is effectively an infinite bath in the model, while proportional decreases in $[Cl^-]_o$ were applied
320 to correct for the changes to charge and osmotic balance. Additions in the extracellular space,

321 similarly, resulted in a temporary depolarization of E_{Cl} and V_m, but no persistent shift in these
322 parameters (**Fig. 4D**). The addition of extracellular impermeant anions did however result in a small
323 compensatory decrease in cell volume secondary to the large shifts in $[Cl^-]_i$ required to maintain the
324 proportion of $[Cl^-]_i$ to $[Cl^-]_o$ according to the Nernst potential. In summary, there is no lasting effect on
325 the reversal potential or driving force for Cl^- if only the concentration of a neuron's intracellular or
326 extracellular impermeant anions is altered.

327

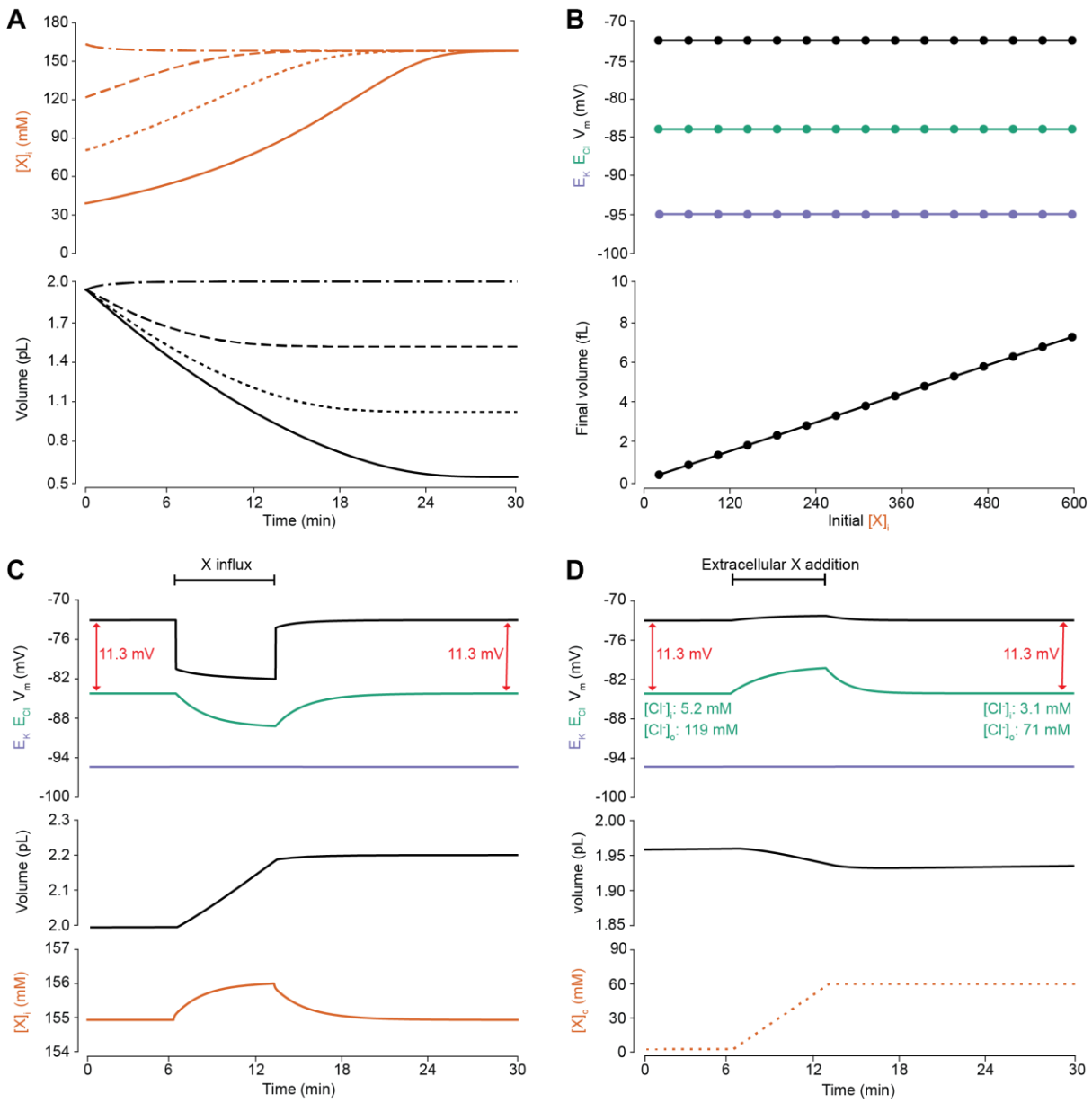

328

329 *Figure 4: Adding intracellular or extracellular impermeant anions, without changing the average*
330 *charge of impermeant anions, does not affect the steady state gradient or driving force for chloride.*
331 *(A) Initiating the model with different starting concentrations of intracellular impermeant anions ($[X]_i$)*
332 *with the same average charge z (orange, top panel), led to compensatory volume changes (bottom*
333 *panel) which resulted in identical steady state concentrations. (B) Steady state E_{Cl} (green), E_K (purple)*
334 *and V_m (black) were identical regardless of initial $[X]_i$. Final volume however was a linear function of*
335 *initial $[X]_i$ (bottom panel). (C) Addition of impermeant anions of the same average charge (z) caused*
336 *transients shifts in E_{Cl} (green, top panel), E_K (purple), V_m (black) as well as $[X]_i$ (orange, bottom panel)*
337 *for the duration of the influx, and sustained increases in volume (black, middle panel). No persistent*
338 *changes in E_{Cl}, E_K or V_m were observed. The full time-dependent ionic and water fluxes for the*
339 *experiment are shown in Figure 4 – figure supplement 1, which shows that the inward flux of*
340 *impermeant anions causes fluxes of all other ions. (D) Similarly, the addition of extracellular*
341 *impermeant anions in an osmoneutral manner causes transient shifts in the permeable ion gradients*
342 *(top panel, colours as in 'C'), and sustained changes in cellular volume (black, middle panel) as well as*
343 *the extracellular X and extracellular and intracellular Cl^- concentrations.*
344
345 Changing the average charge of impermeant anions can drive substantial shifts in the reversal
346 potential for chloride, but has negligible effects on chloride driving force.
347 We next sought to determine how changes in the average charge of the impermeant ions (z) might
348 influence the driving force on Cl^-. Such changes in average z could be associated with various cellular
349 processes, including post-translational modifications of proteins that decrease their charge without
350 changing the absolute number of protein molecules. To investigate this parameter, we modified the
351 average z of intracellular impermeant anions from -0.85 to -1 whilst measuring accompanying changes
352 in E_{Cl}, E_K, V_m and cell (**Fig. 5A**). We found that this shift to a more negative average z resulted in both
353 a transient and persistent decrease in E_{Cl}, E_K and V. Importantly, the shifts in E_{Cl} were accompanied by
354 broadly matching shifts in E_K and V, which resulted in a small change in the driving force for Cl^- of < 0.2

355 mV. Both numerical and analytic calculation of steady state values for E_{Cl}, E_K and V_m in our model
356 showed that changing the average charge of impermeant anions, while substantially affecting E_{Cl}, had
357 very small effects on the driving force for Cl^- (**Fig. 5B**). By shifting z within reasonable ranges for
358 mammalian neurons (Lodish et al., 2009; Raimondo et al., 2015), and assuming osmo- and electro-
359 neutrality, only shifts of < 1 mV could be generated. In addition, although the absolute number of
360 impermeant anions (moles) remained constant throughout the process of modifying z, cell volume
361 shifted, and as a consequence modest alterations to the concentration of impermeant anions
362 occurred as well.
363
364 Next, instead of adjusting the charge of existing anions in intracellular impermeant anions as described
365 above, we directly added impermeant anions of differing valence to the cell (**Fig. 5C and D**). This had
366 the effect of both increasing the absolute quantity of impermeant anions and adjusting the average
367 charge of impermeant anions. The 'addition' of impermeant anions in this way models the *de novo*
368 synthesis of impermeant anion species, or their active transport into the cell. This process also
369 resulted in both transient and persistent changes to E_{Cl}, E_K and V, which was dependent on the extent
370 that average z was altered. Again, whilst the large additions of impermeant anions could substantially
371 alter the Cl^- reversal potential, this had a negligible effect on the driving force for Cl^- due to matching
372 shifts in V_m. Driving shifts in E_{Cl} in this manner also resulted in changes to cell volume (**Figure 5 – figure**
373 **supplement 1**).
374
375 To experimentally test our biophysical modelling predictions, we used photo-activation of ChR2
376 expressing GABAergic interneurons and whole-cell patch clamp recordings of mouse organotypic CA3
377 hippocampal pyramidal neurons to measure V_m, E_{GABA}, and GABA driving force (which approximates
378 Cl^- driving force) before and after addition of impermeant anions (**Fig. 5D**). To add impermeant anions
379 to the recorded cell, we used single cell electroporation of fluorescently tagged anionic dextrans
380 (Alexa Flour 488, see Materials and Methods). Successful addition of impermeant anions could be

381 confirmed visually by observing strong and stable fluorescence of the anionic dextran restricted to the
382 recorded cell (**Fig. 5D, E**). To drive impermeant anions into the cell, negative voltage steps (20 ms, 0.5
383 – 1 V) were applied to the electroporation pipette necessarily resulting in direct membrane
384 depolarization, which recovered over a period of 1-5 minutes (**Fig. 5D**). Once this acute perturbation
385 had settled, as predicted by our model, changing the average charge of impermeant anions, following
386 the addition of highly negatively charged dextrans to the cell, resulted in a stable, mean negative shift
387 in V_m from a baseline of -66.95 ± 3.96 mV to -73.96 ± 3.06 mV (n = 6, *P* = 0.03, *Wilcoxon test,* **Fig. 5E,**
388 **F**). Again in line with our predictions, addition of impermeant anions also resulted in a significant
389 reduction of resting E_{GABA} (a proxy for E_{Cl}) from baseline values of -72.45 ± 1.95 mV to -77.25 ± 1.35
390 mV (*P* = 0.03, *Wilcoxon test*). Importantly, however, similar shifts in V_m and E_{GABA} resulted in an
391 undetectable shift in GABA and hence Cl^- driving force (5.49 ± 4.43 mV vs 3.33 ± 3.46 mV, n = 6, *P* =
392 0.22, *Wilcoxon test,* **Fig. 5E, F**).
393
394 Our single compartment model of Cl^- homeostasis, in conjunction with experimental validation,
395 demonstrates that whilst the adjustment of average impermeant anion charge can significantly affect
396 E_{Cl}, this results in negligible changes to the driving force for Cl^-. This contrasts with the results shown
397 earlier, where adjusting the activity of cation-chloride cotransport modulates both E_{Cl} and the driving
398 force for Cl^- substantially.

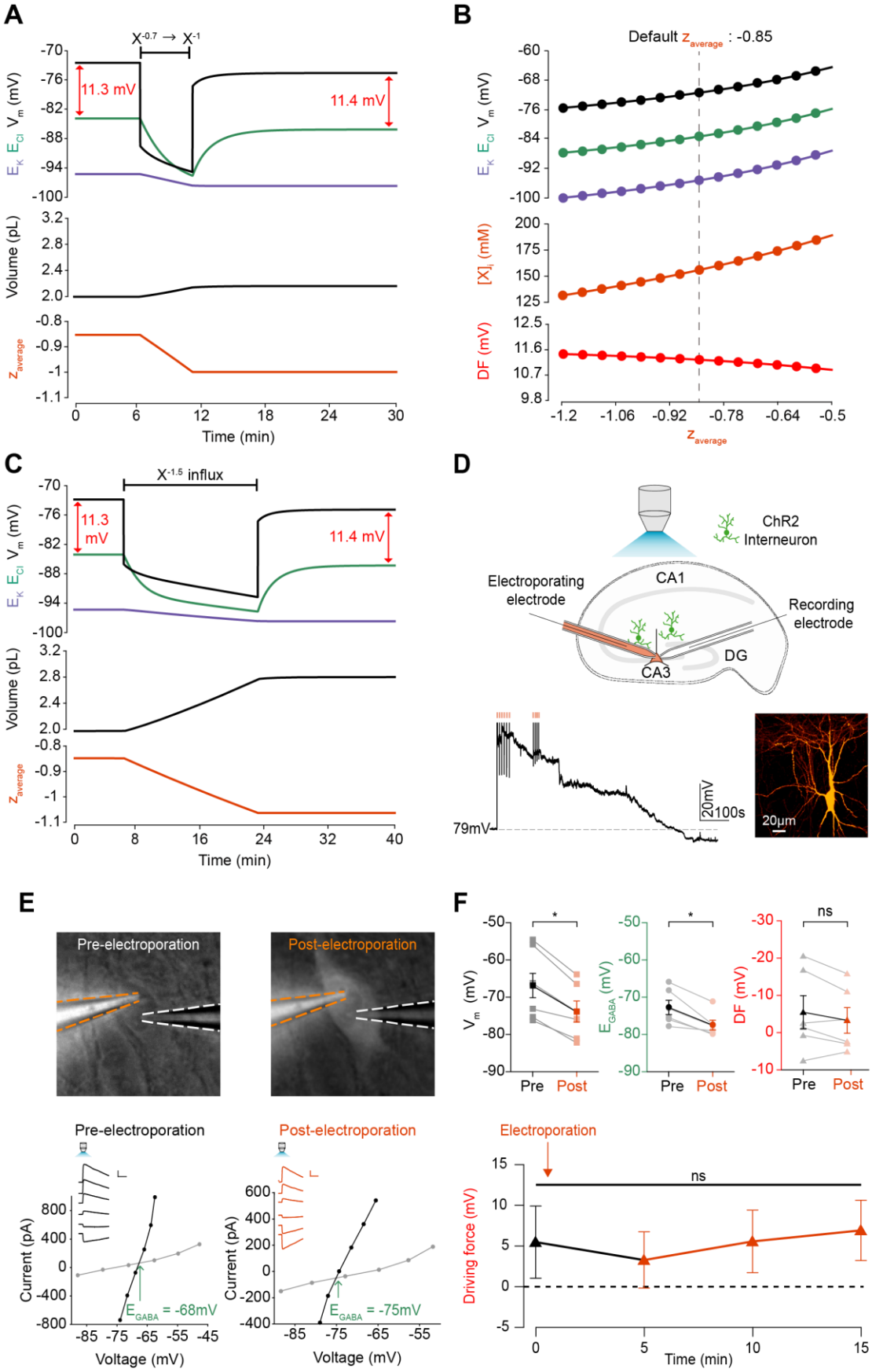
A
X-0.7 → X-1
11.3 mV
11.4 mV
Vm (mV)
EK ECl
Volume (pL)
zaverage
Time (min)
B
Default zaverage : -0.85
Vm (mV)
EK ECl
[X]i (mM)
DF (mV)
zaverage
C
X-1.5 influx
11.3 mV
11.4 mV
Vm (mV)
EK ECl
Volume (pL)
zaverage
Time (min)
D
ChR2
Interneuron
Electroporating electrode
CA1
Recording electrode
DG
CA3
79mV
20mV
100s
20µm
E
Pre-electroporation
Post-electroporation
Current (pA)
Voltage (mV)
EGABA = -68mV
EGABA = -75mV
F
Vm (mV)
EGABA (mV)
DF (mV)
Pre
Post
ns
Electroporation
Driving force (mV)
Time (min)

399

400 *Figure 5: Adjusting the average charge of impermeant anions shifts the chloride reversal potential with*
401 *negligible effects on the driving force for chloride.* *(A) Decreasing the average charge of impermeant*
402 *anions from -0.85 (the default value) to -1 (orange, bottom panel), without changing the absolute*
403 *number of intracellular impermeant anions caused a persistent decrease in E_{Cl} (green, top panel), E_K*
404 *(purple) and V_m with moderate increases in volume (middle panel) in our default single compartment*
405 *model. Negligible changes in Cl^- driving force (ΔDF = 0.16 mV, red) were observed. (B) Analytic solution*
406 *(solid lines) for different impermeant anion average charge (z) exactly matches the steady state values*
407 *from numerical, time series runs (dots) based on adjusting average z as in 'A'. Steady state E_{Cl}, E_K, V_m*
408 *(top panel) and $[X]_i$ (middle) increased with increasing average z, while changes in average z resulted*
409 *in very small changes in Cl^- DF (bottom, red). The vertical dashed line indicates the values at the chosen*
410 *default average z of -0.85. (C) Influx of a species of impermeant anions with average charge -1.5, that*
411 *decreased average z (bottom panel) from -0.85 to -1 and increased the number of impermeant anions*
412 *also caused persistent decreases of E_{Cl}, E_K and V_m as in 'A', but with larger increases in cell volume*
413 *(middle panel). Again, very small persistent changes in Cl^- DF were observed. The volume changes for*
414 *different flux amounts and charges are illustrated in Figure 5 – figure supplement 1. (D) Top, schematic*
415 *of the experimental setup where whole-cell recordings were made from CA3 pyramidal cells in mouse*
416 *organotypic brain slices. Impermeant anions (orange) were delivered via electroporation of the*
417 *negatively charged fluorescent dextran Alexa Flour 488 via a pipette positioned near the soma of the*
418 *recorded cell. $GABA_AR$ currents were elicited via photo-activation (100 ms, 470 nm LED via objective)*
419 *of ChR2-expressing GAD2+ interneurons (green cells) in the presence of 5 µM CGP-35348 to block*
420 *$GABA_BRs$. Lower trace, current clamp recording showing V_m changes during electroporation of anionic*
421 *dextran. Confocal image demonstrating cell-localised fluorescence of the anionic dextran*
422 *electroporated in 'E'. (E) Top, widefield images with electroporation pipette (orange dashed lines) and*
423 *the recording pipette (white dashed lines). Note increased fluorescence in the soma after*
424 *electroporation. Below, insets show $GABA_AR$ currents evoked by photo-activation of GAD2+*
425 *interneurons at different holding potentials. Calibration: 1 s, 100 pA. IV plots were used to calculate*

426 *V_m, E_{GABA} and DF before (left) and after (right) electroporation. (F) Top, population data showing*
427 *significant decreases in mean V_m and E_{GABA} but not DF five minutes after electroporation. Below:*
428 *changes in DF over time. Point at which electroporation occurred marked with orange arrow. 'ns',*
429 *non-significant; *p<0.05.*
430
431 Impermeant anions drive small shifts in chloride driving force by modifying the Na^+/K^+-ATPase pump
432 rate under conditions of active chloride cotransport.
433 We next set out to determine how, and under what conditions, the modification of impermeant
434 anions could potentially generate the very small persistent shifts in Cl^- driving force we observed in
435 our models. Due to their small size (< 1 mV) these were not detectable during the experimental
436 validation. First, we repeated the simulation performed in Figure 5A by changing the average charge
437 of impermeant anions in the cell, but under conditions where the Na^+/K^+-ATPase effective pump rate
438 (J_p) was either a cubic function of the transmembrane Na^+ gradient (default condition) or was fixed at
439 a constant value (**Fig. 6A**). In the case where the pump rate was fixed, adjusting the average charge of
440 impermeant anions generated no persistent change in Cl^- driving force (**Fig. 6A**). Modifying
441 impermeant anions caused a significant change in steady-state intracellular Na^+ concentration when
442 J_p was kept constant. However, small shifts in Cl^- driving force occurred only when the effective pump
443 rate was variable, in which minor changes to $[Na^+]_i$ caused significant changes to J_p, which in turn
444 resulted in a small shift in Cl^- driving force. There is a direct relationship between the average charge
445 of impermeant anions (z), $[Na^+]_i$, the effective Na^+/K^+-ATPase pump rate and Cl^- driving force. This
446 relationship was abolished when the effective Na^+/K^+-ATPase pump rate was held constant by
447 removing its dependence on Na^+ (**Fig. 6B**). In addition, even large variations in effective pump rate
448 near the default value caused negligible shifts in Cl^- driving force of < 1 mV. These results were similar
449 when using the experimentally-matched ATPase model by Hamada et al. (2003), with slight
450 differences in final values (**Figure 6 – figure supplement 1A**). These small, impermeant anion driven,

451 Na^+/K^+-ATPase pump dependent shifts in Cl^- driving force are completely dependent on the presence
452 of cation-chloride cotransport. In the absence of KCC2, there is no Cl^- driving force as $E_{Cl} = V_m$ (**Fig. 6F**).
453
454 We then tested whether relaxing the condition of transmembrane osmoneutrality might also alter
455 impermeant anion induced effects on Cl^- driving force. We modelled a situation where increases in
456 cell surface area beyond a certain 'resting' surface area generated a hydrostatic pressure (membrane
457 tension), which could balance an osmotic pressure difference of 10 mM between the intra and
458 extracellular compartments (see **Fig. 6C**, schematic in **Fig. 6E** and Materials and Methods). In this case,
459 adding impermeant anions of default charge z resulted in constrained increases in cell volume, which
460 were accompanied by persistent transmembrane differences in osmolarity and intracellular Na^+
461 concentration. This was sufficient to generate small differences in driving force for Cl^- of < 0.2 mV for
462 reasonable increases in cell surface area (Nichol and Hutter, 1996; Dai et al., 1998). Again, this was
463 entirely due to Na^+ driven shifts in the Na^+/K^+-ATPase effective pump rate. By removing the
464 dependence of Na^+/K^+-ATPase activity on Na^+ concentration, addition of impermeant anions no longer
465 generated persistent shifts in Cl^- driving force (**Fig. 6C**). Because the model is also directly dependent
466 on $[Na^+]_i$, the results were similar when using the experimentally-matched ATPase model by Hamada
467 et al. (2003) (**Figure 6 – figure supplement 1B**). We observed a direct relationship between
468 transmembrane osmotic gradient, $[Na^+]_i$, the effective Na^+/K^+-ATPase pump rate and Cl^- driving force.
469 This relationship was removed when the effective Na^+/K^+-ATPase pump rate was held constant, with
470 no changes in Cl^- driving force seen despite the generation of the same shift in the transmembrane
471 osmotic gradient (**Fig. 6D**).
472
473 In summary, changes in Cl^- driving force generated by changing the ionic contributions to cellular
474 charge (by altering the average charge of impermeant anions) or osmoneutrality (by increasing the
475 contribution of hydrostatic pressure) are due to the alteration of the dynamics of active ion transport
476 mechanisms in the cell. However, these effects are negligible in magnitude and cannot contribute

477 significantly to setting physiologically observed Cl^- driving forces. It is worth reiterating that any non-

478 zero Cl^- driving force is entirely dependent on the presence of active Cl^- cotransport. In our model, in

479 the absence of KCC2, neither the Na^+/K^+-ATPase nor impermeable anions can shift Cl^- out of

480 equilibrium (**Fig. 6F**).

481

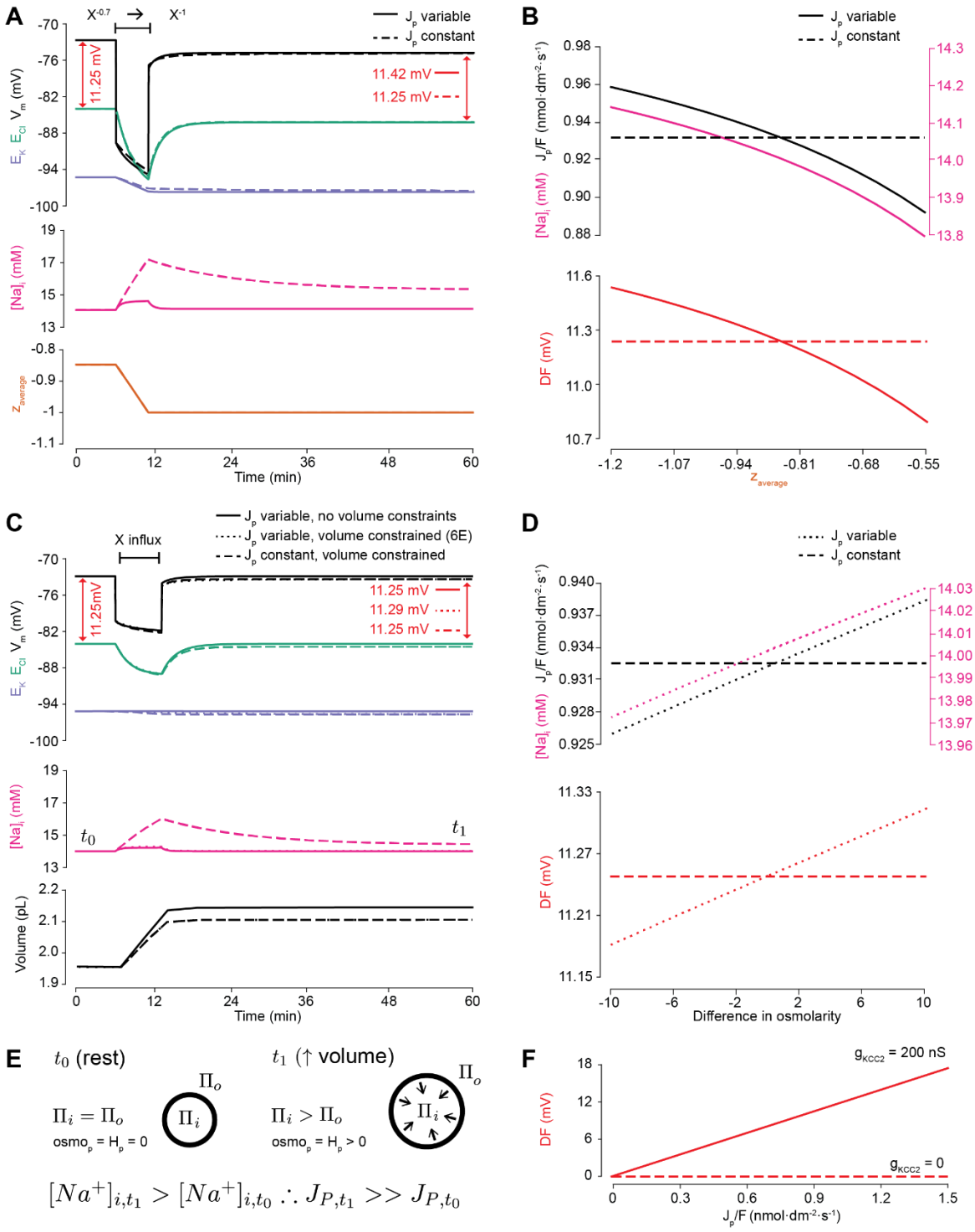

482

483 Figure 6: Impermeant anions drive small shifts in chloride driving force by modifying the Na^+/K^+-
484 ATPase pump rate under conditions of active chloride cotransport. *(A) E_{Cl} (green), E_K (purple) and V_m*
485 *(black) (top panel), $[Na^+]_i$ (pink, middle panel) and average impermeant anion charge z (orange, lower*
486 *panel) over time in the default single compartment model. Changing the average z from -0.85 to -1*
487 *generated small, persistent Cl^- driving force (DF) shifts (arrows, red) only when the effective ATPase*
488 *pump rate (J_p) was variable (solid line) and not when J_p was kept constant (dashed line). (B) Solving*
489 *analytically across different values of z with either a variable J_p (solid lines) or a constant J_p (dashed*
490 *line), demonstrates the direct relationship between Na^+ (pink), effective pump rate (J_p) (top panel) and*
491 *DF (lower panel, red). (C) E_{Cl} (green), E_K (purple) and V_m (black) (top panel), $[Na^+]_i$ (pink, middle panel)*
492 *and cell volume (black, lower panel) over time in the default single compartment model. Impermeant*
493 *anions of the same average charge of the cell were added. A volume constraint was incorporated by*
494 *adding a hydrostatic force dependent on membrane tension (dashed lines), which resulted in an*
495 *impermeable anion induced transmembrane osmotic differential. This caused a small change in DF*
496 *when J_p was variable (dashed line), but not when J_p was held constant (dotted lines). (D) Solving*
497 *analytically across osmolarity differences demonstrates the direct relationship between Na^+ (pink),*
498 *effective pump rate (J_p) (top panel) and DF (lower panel). Note, the small changes in DF. (E) Schematic*
499 *explaining the mechanism through which impermeant anion induced cell swelling in the presence of*
500 *volume constraints (i.e. membrane tension) result in steady states with equal but non-zero osmotic*
501 *($osmo_P$) and hydrostatic pressures (H_P), causing transmembrane osmotic differences (t_1). This causes*
502 *small changes in Na^+, and hence J_p. (F) All Na^+/K^+-ATPase pump rate-related shifts in the DF require*
503 *KCC2 activity; in the absence of activity (dashes), no shifts in driving force can occur. In Figure 6 –*
504 *supplement figure 1, we show that the results in (A) and (C) are similar when an experimentally-*
505 *matched model of the Na^+/K^+-ATPase is used.*
506

507 Changes in cation-chloride cotransport activity generate local differences in chloride reversal and
508 driving force, which depend on cytoplasmic diffusion rates.
509 An important functional question is how Cl^- driving force might be modified at a local level within a
510 neuron. We considered local persistent changes of Cl^- driving force for the case of active
511 transmembrane Cl^- fluxes (**Fig. 7**) and impermeant anions (**Fig. 8**) by extending the single compartment
512 model described above into a multi-compartment model or 'virtual dendrite.' This dendrite was 100
513 µm in length and consisted of ten compartments, each of 10 µm length and 1 µm diameter. The
514 compartments contained the same mechanisms and default parameterization as the single
515 compartment model described above. Compartmental volume was changed by altering the radius,
516 while holding the length constant. In addition, all ions, except impermeant anions, could move
517 between compartments by electrodiffusion (**Fig. 7A** and Materials and Methods).
518
519 To explore the local effects of CCC activity, we increased g_{KCC2} from our default value of 20 µS/cm^2 to
520 600 µS/cm^2 in the second last compartment of the virtual dendrite exclusively. This resulted in a
521 persistent decrease in E_{Cl}, concurrent with a modest decrease in V_m, resulting in a permanent increase
522 in Cl^- driving force and minimal change in compartment volume (**Fig. 7B**). The spatial precision of this
523 alteration depended strongly on the diffusion constant for Cl^-. With a Cl^- diffusion constant of
524 2.03×10^{-7} dm^2.s^{-1}, these alterations spread widely through the virtual dendrite. For example, the
525 change in Cl^- driving force was 4.8 mV in the furthermost compartment (90 µm apart) as compared to
526 5.9 mV in the compartment manipulated. When we decreased the Cl^- diffusion constant by one order
527 of magnitude, the change in Cl^- driving force was 7.3 mV in the compartment in which KCC2 was
528 adjusted, but only 1.8 mV in the furthermost compartment from the site of manipulation (**Fig. 7C**).
529 These findings suggest that local differences in cation-chloride cotransport activity can drive spatially
530 restricted differences in Cl^- driving force under conditions of constrained Cl^- diffusion, however under
531 conditions of typical ionic diffusion the effect of Cl^- transport by KCC2 is relatively widespread.
532

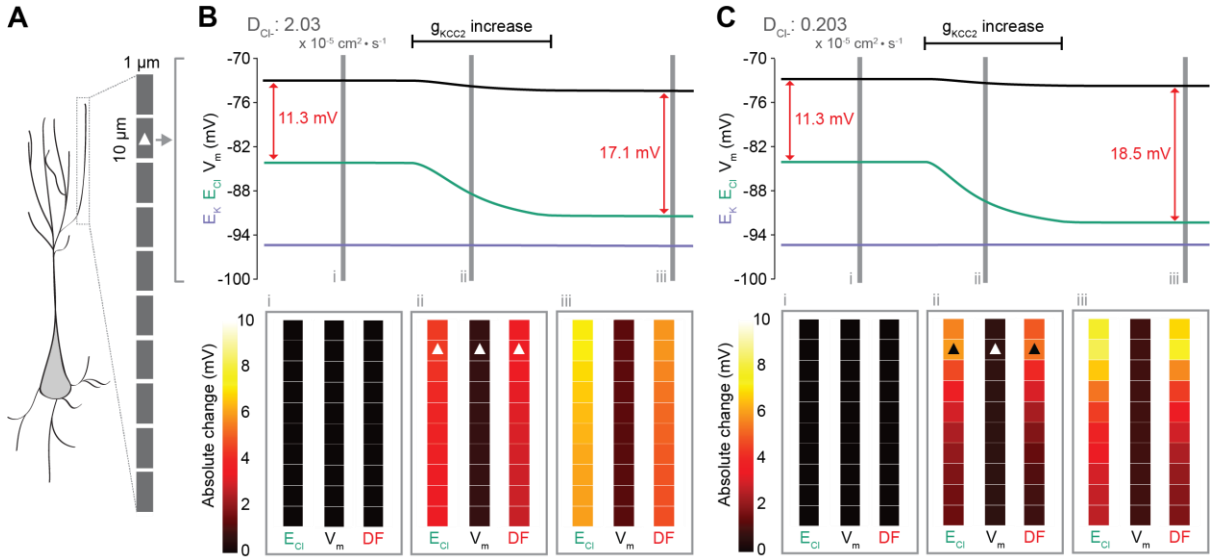

533

534 *Figure 7: Local changes in KCC2 activity generate local differences in chloride reversal and driving force*

535 *only under conditions of constrained chloride diffusion. (A) Schematic depicting the multi-*

536 *compartment model representing a virtual dendrite of length 100 µm. The virtual dendrite consists of*

537 *10 compartments of length 10 µm and initial radius 0.5 µm. Each compartment contains the same*

538 *mechanisms and default parameterization as the single compartment model. All ions, except*

539 *impermeant anions, could move between compartments by electrodiffusion. (B) Top panel, E_{Cl} (green),*

540 *E_K (purple), V_m (black) and calculated DF (arrows, red) from the 2nd from top compartment (indicated*

541 *with a white triangle) where the conductance of KCC2 was increased. The insets depict the diameter,*

542 *and absolute change from baseline of E_{Cl}, V_m and DF for all compartments before (i), during (ii) and*

543 *after (iii) the activity of KCC2 was selectively increased. This resulted in E_{Cl} decreasing in all*

544 *compartments with minimal changes to E_K and V. Consequently, the Cl^- DF (red) increased. In this case*

545 *the diffusion constant for Cl^- (D_{Cl} = 2.03 x 10^{-7} $dm^2.s^{-1}$) resulted in E_{Cl} and DF changes being widespread*

546 *across the virtual dendrite. (C) Reducing the Cl^- diffusion constant to 0.2 x 10^{-7} $dm^2.s^{-1}$ resulted in a*

547 *localized effect of compartment specific KCC2 activity increases on E_{Cl} and DF.*

548

549 Local impermeant anions do not appreciably affect the local driving force for chloride.

550 Following the last result, we considered whether changing impermeant anions in part of a dendrite

551 could create a local area with a different Cl^- driving force compared to the rest of the cell. We first

552 added impermeant anions of average charge (z) exclusively to the second-last compartment of the
553 virtual dendrite while measuring the Cl^- reversal, V_m and Cl^- driving force in all compartments. During
554 addition of the impermeant anions, E_{Cl} and V_m decreased with an accompanying decrease in Cl^- driving
555 force. However, following cessation of impermeant anion influx, all parameters returned to baseline
556 levels, except for the volume of that specific compartment, which showed a modest increase (**Fig. 8B**).
557 This suggests that local addition of impermeant anions of average charge has no local effect on Cl^-
558 homeostasis but can affect the volume of the compartment concerned.
559
560 Next, we again added impermeant anions to the second-last compartment of the virtual dendrite, but
561 this time we added impermeant anions with a more negative charge than average (z = -1). This
562 resulted in the average charge of impermeant anions in that specific compartment becoming more
563 negative (**Fig. 8C**). During the addition of the impermeant anions, E_{Cl} and V_m decreased across the
564 dendrite, but with small accompanying shifts in Cl^- driving force. Following cessation of local
565 impermeant anion influx, a persistent shift in E_{Cl} and V_m was observed specifically in the compartment
566 manipulated. However, this generated a negligible, persistent change in Cl^- driving force (< 0.01 mV
567 change in driving force for a compartment specific change in z from -0.85 to -0.93), and only within
568 that specific compartment of the virtual dendrite. Again, impermeant anion addition resulted in a
569 permanent increase in the volume of the compartment concerned. This finding suggests that local
570 impermeant anions can adjust the Cl^- reversal potential locally, but are not well-placed to cause
571 significant, permanent shifts in the driving force for Cl^-. Indeed, electrodiffusion may further limit the
572 degree to which changes in impermeant ion charge can modify driving forces through alterations in
573 active ionic transport: the resulting permanent Cl^- driving force changes in the multi-compartment
574 model are many times smaller than the shifts in the single compartment version (as compared to **Fig.**
575 **6B**).
576

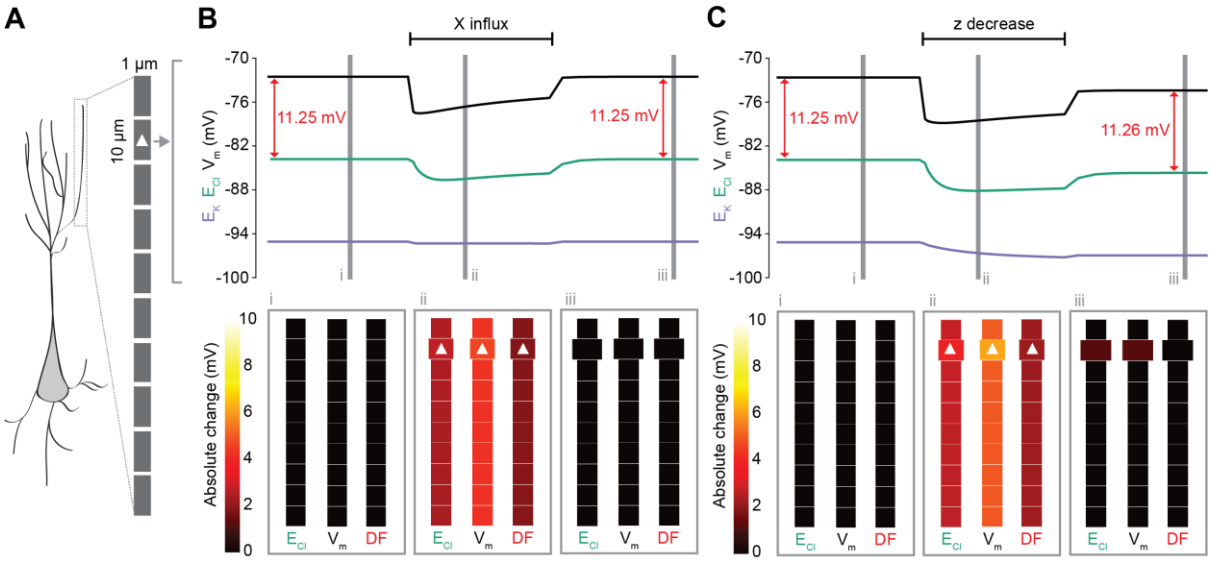

577

578 *Figure 8: Local changes in impermeant anions do not establish the local driving force for chloride.* *(A)*

579 *Multi-compartment model of a 10 compartment 100 µm virtual dendrite as in Figure 7. (B) Top panel,*

580 *E_{Cl} (green), E_K (purple), V_m (black) and calculated DF (arrows, red) within the compartment where*

581 *additional impermeant anions were exclusively added (indicated with a white triangle). The insets*

582 *depict the diameter, and absolute change from baseline for E_{Cl}, V_m and DF for each compartment of*

583 *the virtual dendrite before (i), during (ii) and after (iii) impermeant anions were added. The selective*

584 *addition of impermeant anions of average z to the 2nd from top compartment resulted in transient but*

585 *non-permanent shifts in E_{Cl}, V_m and the Cl^- DF in all compartments. The volume of the compartment*

586 *where impermeant anion addition occurred increased permanently. (C) Traces and insets as in 'B'*

587 *showing the addition of impermeant anions of different charge in order to decrease average z in the*

588 *2nd from top compartment specifically. Note that during addition of impermeant anions, E_{Cl}, E_K, V_m*

589 *changed. We also observed persistent decreases in E_{Cl} and V_m in the compartment manipulated, with*

590 *a negligible change in DF (0.01 mV). Again, impermeant anion addition resulted in an increase in the*

591 *volume of the specific dendritic compartment manipulated.*

592 *Discussion*

593 The driving force for Cl^- is a fundamental parameter affecting the excitability of neuronal networks
594 (Raimondo et al., 2017). Recently, impermeant anions, rather than CCCs, have been suggested as the
595 primary determinants of the neuronal driving force for Cl^- (Glykys et al., 2014). Here we have explored
596 the determinants of the Cl^- driving force in neurons by deriving theoretical models based on
597 biophysical first principles. We show that the Na^+/K^+-ATPase, baseline K^+, Na^+ and Cl^- conductances,
598 average charge on impermeant anions, water permeability and CCCs, likely all play roles in setting
599 neuronal $[Cl^-]_i$. However, our findings suggest that while impermeant anions can contribute to setting
600 the $[Cl^-]_i$ in neurons, they can only affect Cl^- driving force by modifying the activity of active transport
601 mechanisms (i.e. the Na^+/K^+-ATPase). Our modelling and experimental data demonstrate that under
602 physiologically relevant conditions, impermeant anions do not alter the Cl^- driving force significantly.
603 In contrast, CCCs are well placed to modulate Cl^- driving force and hence inhibitory signaling.

604

605 Previous theoretical models, which account for the dynamics of Cl^- ions, have been useful in
606 determining how changes to the driving force for Cl^- are critical for controlling the effect of synaptic
607 inhibition in the brain (Qian and Sejnowski, 1990; Staley and Proctor, 1999; Doyon et al., 2011; Jedlicka
608 et al., 2011; Lewin et al., 2012; Mohapatra et al., 2016). Whilst these models have included the Na^+/K^+-
609 ATPase, the interacting dynamics of several ion species, CCCs (Doyon et al., 2011; Krishnan and
610 Bazhenov, 2011), electrodiffusion (Qian and Sejnowski, 1989) and impermeant anions and volume
611 regulation (Dijkstra et al., 2016), none have combined all of these mechanisms to explore how their
612 combination determines the local driving force for Cl^-. Our theoretical approach is based on the pump-
613 leak formulation (Tosteson and Hoffman, 1960). It suggests that mammalian cells maintain their
614 volume under osmotic stress generated by impermeant anions and the Donnan effect by employing
615 active transport of Na^+ and K^+ using the Na^+/K^+-ATPase (Armstrong, 2003; Kay, 2017). A Donnan
616 equilibrium, a true thermodynamic equilibrium requiring no energy to maintain it, is not possible in
617 cells with pliant membranes like neurons (Sperelakis, 2012).

618

619 Our model conforms to the pump-leak formulation: abolishing the activity of the Na^+/K^+-ATPase leads
620 to cell swelling, progressive membrane depolarization and rundown of ionic gradients, including that
621 of Cl^-. Therefore, the Na^+/K^+ ATPase is a fundamental cellular parameter that stabilizes cell volume and
622 determines all ionic gradients including that of Cl^- and hence must be considered in any attempt to
623 model ion homeostasis. Interestingly however, we demonstrate that above a certain level of Na^+/K^+-
624 ATPase activity, even many fold changes in pump rate have minimal effects on volume, E_{Cl} and V_m.
625 This might explain recent experimental findings in which periods of Na^+/K^+ ATPase inhibition using
626 ouabain caused modest changes to cell volume (Glykys et al., 2014). It therefore seems unlikely that
627 neurons adjust the Na^+/K^+-ATPase as a means for modulating Cl^- driving force.

628

629 Baseline ion conductances are another important factor that affect Cl^- driving force. Our model is
630 consistent with recent experimental results that demonstrate that increased neuronal Na^+
631 conductance (for example by activating NMDA receptors, or preventing closure of voltage-gated Na^+
632 channels), leads to progressive neuronal swelling, membrane depolarization and Cl^- accumulation
633 (Rungta et al., 2015) – the primary pathological process in cytotoxic oedema (Liang et al., 2007). We
634 also show that tonic neuronal Cl^- conductance only affects baseline $[Cl^-]_i$ and driving force in the
635 presence of CCCs. Without active Cl^- flux, which CCCs provide, there is no driving force for passive Cl^-
636 flux and hence no mechanism for $[Cl^-]_i$ changes resulting from selective modification of a Cl^-
637 conductance. This is consistent with both classic (Misgeld et al., 1986; Thompson and Gähwiler, 1989)
638 and recent experimental findings (Berglund et al., 2016).

639

640 In our model, we find that elevating the activity of KCC2, the most active CCC in mature neurons (Ben-
641 Ari, 2002), increases the driving force for Cl^- by shifting the reversal potential for Cl^- closer to that of
642 K^+. Interestingly, large shifts (~7 mV) in driving force were associated with very minor (1%) changes in
643 volume or membrane potential. As such, modulating KCC2 represents a specific means for

644 manipulating the neuronal Cl^- driving force. This is consistent with traditional dogma, recent and
645 previous experimental results (Kaila et al., 2014; Klein et al., 2017) as well as our own experimental
646 validation using furosemide to block the activity of KCC2, which drove significant changes in driving
647 force with little effect on V_m. In further support of this, our meta-analysis of numerous experimental
648 studies showed a strong correlation between change in KCC2 expression and Cl^- driving force, but not
649 between KCC2 expression and V_m. There is an ongoing debate as to whether some cotransporters,
650 including CCCs, might also couple water transport to ion transport (Zeuthen, 1994; MacAulay et al.,
651 2002; Gagnon et al., 2004; Charron et al., 2006). Although we did not model the active movement of
652 water by KCC2, this scenario would not alter the central importance of CCCs for setting the Cl^- driving
653 force.
654
655 Using our multi-compartment model, which incorporated electrodiffusion, we found that local
656 modification of KCC2 activity has a specific local effect on Cl^- driving force that is dependent on the
657 characteristics of intracellular Cl^- diffusion. Cytoplasmic Cl^- diffusion rates had to be reduced
658 substantially before we observed local changes in Cl^- driving force driven by KCC2 (Qian and Sejnowski,
659 1989; Kuner and Augustine, 2000). Whilst differences in KCC2 activity might generate a gradient in Cl^-
660 driving force between large subcellular structures (i.e. dendrites versus soma), our modelling results
661 call into question the idea of synapse-specific regulation of Cl^- driving force within the same cellular
662 domain (Földy et al., 2010).
663
664 Glykys et al. (2014) used Cl^- imaging and various experimental manipulations to claim that $[X]_i$ and $[X]_o$
665 sets $[Cl^-]_i$ and the Cl^- driving force. From our theoretical analysis, we find that modifying the amount
666 of impermeant anions inside or outside neurons has no persistent effect on $[Cl^-]_i$ or Cl^- driving force,
667 unless we include a mechanism that allows a transmembrane osmotic pressure differential to develop
668 that indirectly affects active transport mechanisms. Even in this case, under transmembrane pressure
669 differentials that do not lyse the membrane (Nichol and Hutter, 1996), Cl^- driving force changes are

670 negligible (< 1 mV). Recently it has been suggested that the viscoelastic properties of the cellular
671 cytoskeleton could allow it to take up osmotic shifts created by impermeant anion movement like a
672 sponge (Sachs and Sivaselvan, 2015). This would mean that one would not see as large a volume shifts
673 as predicted by our models. In our model we have assumed that water can pass through the neuronal
674 membrane to equalize osmotic differences. Although it is thought that some neurons do not express
675 aquaporin channels (Andrew et al., 2007), water can permeate the phospholipid bilayer (Fettiplace
676 and Haydon, 1980). Therefore, whilst differences in neuronal water permeability might affect the time
677 taken to reach steady-state, the steady state values themselves are unlikely to be affected. We
678 conclude that $[Cl^-]_i$ and the Cl^- driving force are not determined by the *concentration* of impermeant
679 anions.
680
681 However, our theoretical findings offer a potential explanation for recent experimental observations.
682 We show that modifying the average *charge* upon impermeant anions (i.e. z in $[X^z]_i$), rather than their
683 concentration, can affect $[Cl^-]_i$ and E_{Cl-}. Relating this to prior experimental observations, Glykys et al.
684 (2014) used SYTO64 staining of nucleic acids and perfusion of weak organic acids in conjunction with
685 Cl^- imaging to suggest that $[Cl^-]_i$ depends upon internal impermeant anions ($[X]_i$). If such a manipulation
686 modifies the average charge on internal impermeant anions, and not concentration *per se*, this could
687 account for the observed changes in $[Cl^-]_i$. Glykys et al. (2014) did not measure V_m or the Cl^- driving
688 force in these experiments. The clear prediction from our model is that any manipulation, which
689 changes the average charge of impermeant anions would not appreciably affect the Cl^- driving force
690 because any impermeant anion driven change on E_{Cl-} is matched by an equivalent effect on V_m due to
691 accompanying shifts in cation concentrations. We have provided experimental support for this
692 prediction by showing that whilst E_{GABA} (and E_{Cl}) can be shifted by addition of impermeant anions using
693 electroporation of membrane impermeant anionic dextrans, V_m is shifted in a similar direction
694 resulting in an undetectable change in Cl^- driving force.
695

696 Given prior theoretical predictions (Kaila et al., 2014; Voipio et al., 2014; Savtchenko et al., 2017), it is
697 interesting that our model reveals that changing impermeant anions could affect the Cl^- driving force
698 at all. We found that the small (< 1 mV) impermeant anion-driven changes in Cl^- driving force observed
699 in our model were caused by indirect effects on Na^+ concentration and hence Na^+/K^+-ATPase activity.
700 The impermeant anion-driven changes in Cl^- driving force are even smaller in the multi-compartment
701 model (< 0.1 mV), in which electrodiffusion allows local changes in Na^+ to dissipate. When Na^+/K^+-
702 ATPase activity was decoupled from the transmembrane Na^+ gradient, we found that impermeant
703 anions were unable to cause persistent shifts in Cl^- driving force as predicted theoretically (Kaila et al.,
704 2014; Voipio et al., 2014; Savtchenko et al., 2017). It is important to note that these small, impermeant
705 anion-Na^+/K^+-ATPase-driven shifts in Cl^- driving force are dependent on the presence of cation-
706 chloride cotransport in the form of KCC2 and would entail changes in energy use by the Na^+/K^+-ATPase.
707 In other words, active transport mechanisms are again required to drive changes in Cl^- homeostasis.
708
709 In summary, our theoretical models, which are derived from well-established physical principles, are
710 consistent with our own experimental data and that of others (Glykys et al., 2014; Kaila et al., 2014;
711 Klein et al., 2017), and suggest that impermeant anions alone cannot shift Cl^- out of equilibrium across
712 the neuronal membrane. Were neurons to alter impermeant anion concentrations or charge, the
713 resting membrane potential would be modified with little effect on the Cl^- driving force. Our work
714 confirms the central importance of CCC activity in determining the effects of inhibitory synaptic
715 transmission in the nervous system.

716 *Materials and methods*

717 *Single compartment model.* The single compartment model consisted of a cylindrical semi-permeable
718 membrane separating the extracellular solution from the intracellular milieu with variable volume
719 (**Fig. 1A**). The extracellular ionic concentrations were assumed constant (**Table 1**). Permeable ions in
720 the model were K^+, Na^+ and Cl^- with their usual charges, while impermeant anions X were assumed to
721 be a heterogeneous group of impermeant chemical species with average intracellular charge z and
722 extracellular charge -1. z was chosen on the basis of known resting intracellular ion concentrations
723 (Lodish et al., 2009; Raimondo et al., 2015) and osmolarity (Π). Bicarbonate ions were not included in
724 our model as a permeant anion as they were assumed to be important for acute depolarizing effects
725 (via $GABA_A$Rs) rather than the chronic shifts in Cl^- driving force, which are the focus of this work (Staley
726 and Proctor, 1999). The model included ionic leak currents for the permeable ions, Na^+/K^+-ATPase
727 transporters and a CCC, in this case the K^+-Cl^- cotransporter (KCC2). KCC2 and not NKCC1 is thought to
728 be the most active CCC in mature neurons (Ben-Ari, 2002), therefore, to maintain conceptual simplicity
729 only KCC2 was modelled. Cell volume (w) change was based on osmotic water flux and incorporated
730 a membrane surface area scaling mechanism. An analytical solution to the model at steady state was
731 derived using standard techniques and can be found in Supplementary file 1. The numerical model
732 was initialised assuming conditions close to electroneutrality and an osmotic equilibrium between the
733 intracellular and extracellular compartments. A forward Euler approach was used to update variables
734 at each time step (dt) of 1 ms. Using a smaller dt did not influence the results in Figure 1-5. Code was
735 written in Python 2 and is available on GitHub (https://github.com/kiradust/model-of-neuronal-
736 chloride-homeostasis). The GitHub repository includes a file of Supplementary figures, in which we
737 display transmembrane fluxes of all ions and water for relevant simulations. An example figure
738 displaying ionic flux for all ions is available for Figure 4C in Figure 4 – figure supplement 1.

739

740 *Membrane potential.* The membrane potential V_m was based on the "Charge Difference" approach of
741 Fraser and Huang (2004) as follows:

742

$$V_m = \frac{F\,([Na^+]_i + [K^+]_i - [Cl^-]_i + z[X^z]_i)}{C_m A_m} \quad (1)$$

743

744 where F is Faraday's constant, C_m is the unit membrane capacitance and A_m is calculated as the ratio
745 of the surface area (of the cylinder) to cell volume. The term in brackets is the sum of all ionic charges
746 within the cell. This approach has the advantage that the initial voltage can be calculated without
747 needing to assume a steady state as is required for by the Goldman-Hodgkin-Katz (GHK) equation.

748

749 *Permeable ion concentrations.* Intracellular concentrations of the permeable ions Na^+, K^+ and Cl^- were
750 updated individually by summing trans-membrane fluxes. Leak currents were calculated using the
751 standard equivalent circuit formulation $I = g(V_m - E)$. In addition, Na^+ and K^+ were transported
752 actively by the Na^+/K^+-ATPase, with pump rate J_p, which was approximated by a cubic function
753 dependent on the transmembrane sodium gradient, following Keener and Sneyd (1998):

754

$$J_p = \mathrm{P}\left(\frac{[Na^+]_i}{[Na^+]_o}\right)^3, \quad (2)$$

755

756 where P is the pump rate constant. Because it is a function of the sodium gradient, J_p decreases as
757 $[Na^+]_i$ depletes. This formulation has been shown to be similar to more accurate kinetic models reliant
758 on both the Na^+ gradient and ATP concentration (Keener and Sneyd, 1998). To switch the ATPase
759 pump on or off (**Fig. 1C**), P was decreased/increased exponentially over 10-20 minutes, consistent
760 with previous reports of the dynamics of inhibition of the ATPase by ouabain and in turn the inhibition
761 of ouabain's effects by potassium canrenoate (Baker and Willis, 1972; Yeh and Lazzara, 1973). The
762 ATPase pumps 2 K^+ ions into the cell for every 3 Na^+ ions out and these constants must be multiplied
763 by J_p for each ion respectively. K^+ and Cl^- were also modified by flux through the type 2 K-Cl
764 cotransporter (KCC2), J_{KCC2} (Doyon et al., 2016):

$$J_{KCC2} = g_{KCC2}(E_K - E_{Cl}), \tag{3}$$

where g_{KCC2} is a fixed conductance and E_K and E_{Cl} are the Nernst potentials for K^+ and Cl^- respectively. J_{KCC2} is 0 when E_K=E_{Cl}. The rate of change of the intracellular concentration of the three permeant ions was given by the following equations, with the Nernst potentials for each ion given by $E_{ion} = \frac{RT}{zF}\ln\left(\frac{[ion]_{out}}{[ion]_{in}}\right)$, w indicating the cell volume, and $\frac{dw}{dt}$ as described in equation (7) (**Fig. 1-5, 6A, B, 7 and 8**) or (9) (**Fig. 6C-E**):

$$\frac{d[Na^+]_i}{dt} = -\frac{A_m}{F}\left(g_{Na}(V_m - E_{Na}) + 3J_p\right) - \frac{1}{w}\frac{dw}{dt}[Na^+]_i \tag{4}$$

$$\frac{d[\mathrm{K}^+]_i}{dt} = -\frac{A_m}{F}\left(g_K(V_m - E_K) - 2J_p - J_{KCC2}\right) - \frac{1}{w}\frac{dw}{dt}[K^+]_i \tag{5}$$

$$\frac{d[\mathrm{Cl}^-]_i}{dt} = \frac{A_m}{F}\left(g_{Cl}(V_m - E_{Cl}) + J_{KCC2}\right) - \frac{1}{w}\frac{dw}{dt}[Cl^-]_i. \tag{6}$$

Volume. Because the osmotic flux of water is expected to be faster than ion fluxes, the volume of the cell was adjusted to preserve transmembrane osmotic balance at each time step. Change in compartment volume, w, was calculated by changing the previous volume proportional to the difference between intracellular and extracellular osmolarity, Π_i and Π_o respectively (Hernández and Cristina, 1998), where v_w is the partial molar volume of water, p_w the osmotic permeability of a biological membrane and SA the surface area:

$$\frac{dw}{dt} = v_w \cdot p_w \cdot SA \cdot (\Pi_i - \Pi_o). \tag{7}$$

For the calculations in Figure 6C-E, where we allowed transmembrane differences in osmolarity to develop, we assumed that at rest the cylindrical cell had a radius of r_a and zero pressure across the membrane, and that the tension (T) in the membrane followed Hooke's law such that the tension was proportional to the difference between the dynamic circumference of the cell and that of the resting state. From Laplace's law the hydrostatic pressure in the cell was given by:

$$H_p = \begin{cases} 4\pi k_m \left(1 - \frac{r_a}{r}\right) & r > r_a \\ 0 & , \ otherwise \end{cases} \tag{8}$$

where k_m is the spring constant of the membrane (Sachs and Sivaselvan, 2015). Equation (7) was thus reformulated:

$$\frac{dw}{dt} = v_w \cdot p_w \cdot SA \cdot \left(\Pi_i - \Pi_o - \frac{H_p}{RT}\right). \tag{9}$$

In order to simulate extreme conditions of constrained volume, a larger k_m was employed than is realistic (Dai et al., 1998). Intracellular ion concentrations were updated again after volume change at each time step. Volume changes were manifested in the cylindrical compartment as change in the radius. In Figure 1-6, the cell was initialised with diameter 10 µm and length 25 µm.

Anion flux. Impermeant anions were manipulated in the compartment in Figure 4-6 and Figure 8 through several mechanisms. Anions could be added to the compartment at a constant rate dependent on A_m and have either the same average intracellular X charge z = -0.85 (**Fig. 4C, 6C and**

805 **8B**), or a different charge (**Fig. 5C, 6A and 8C**). In these cases, the number of moles of X in the
806 compartment was increased. Alternatively, the charge of a species of intracellular X was slowly
807 changed imitating a charge-carrying trans-membrane reaction (**Fig. 5A and 6A**). In this case, the
808 number of moles of intracellular X did not change and it was assumed charge imbalance was mopped
809 up by the extracellular milieu. Finally, extracellular X^- was changed in Figure 4D by removing as much
810 Cl^- as X^- was added, thus maintaining osmolarity and electroneutrality in the extracellular space.
811
812 *Multi-compartment model.* The single compartment dendrite model was incorporated in a multi-
813 compartment model by allowing electrodiffusion to occur between individual compartments
814 operating as described above. Compartments were initialised with a radius of 0.5 µm and length of 10
815 µm. Compartments were linked linearly without branching; 10 connected compartments in total were
816 used. The time step dt was decreased to 10^{-3} ms for simulations in multiple compartments. Code was
817 written in Python 3 and is available on GitHub (https://github.com/kiradust/model-of-neuronal-
818 chloride-homeostasis).
819
820 *Electrodiffusion.* The Nernst-Planck equation (NPE) was used to model one-dimensional
821 electrodiffusion, based on Qian and Sejnowski (1989). The NPE incorporates fluxes because of
822 diffusion and drift (i.e. the movement of ions driven by an electric field). It has been shown to be more
823 accurate than using $J_{diffusion}$ alone in small structures like dendrites (Qian and Sejnowski, 1989). The
824 NPE for J the flux density of ion C is calculated as:
825

$$J = -D\frac{zF^2}{RT}[C]\frac{dV_m}{dx} - DF\frac{d[C]}{dx}, \quad (10)$$

826
827 where D is the diffusion constant of ion C (**Table 1**), z is its charge, [C] is its concentration and x is the
828 distance along the longitudinal axis over which electrodiffusion occurs. The NPE was implemented
829 between compartments i and i+1, assuming the i→i+1 direction was positive, using a forward Euler

approach. The midpoints of the compartments were used to calculate dx, i.e. $dx = \frac{h_i + h_{i+1}}{2}$, and the concentrations of C in each compartment were averaged to obtain J_{drift}, ensuring that $J_{i \to i+1} = J_{i+1 \to i}$, where the fluxes had units of mol/(s.dm^2):

$$J_{i \to i+1} = -D \left(\frac{zF}{RT} \frac{([C]_i + [C]_{i+1})}{2} \frac{dV_m}{dx} + \frac{d[C]}{dx} \right). \quad (11)$$

The flux was multiplied by the surface area between compartments and then divided by compartment volume to determine the flux in terms of molar concentration (M/s), i.e. $\frac{\pi r^2}{\pi r^2 h_i} = \frac{1}{h_i}$, and finally implemented numerically with a forward Euler approach. The implementation mirrored that in Qian and Sejnowski (1989) for non-branching dendrites, but was adjusted for compartments whose volumes can change:

$$C_{i \to i+1} = -\frac{dt}{h_i} D \left(\frac{zF}{RT} \frac{([C]_i + [C]_{i+1})}{2} \frac{\left(V_{m_i} - V_{m_{i+1}}\right)}{dx} + \frac{([C]_i - [C]_{i+1})}{dx} \right). \quad (12)$$

Systematic review. A literature search was performed to identify experimental studies that aimed to correlate a change in KCC2 expression with changes in $[Cl^-]_i$. The MEDLINE database was used and accessed via the PubMed online platform. Search terms included 'chloride', 'Cl', 'intracellular', 'KCC2', 'cotransporter', 'neuronal', 'GABA' using appropriate Boolean operators. All 26 studies that demonstrated changes in KCC2 expression and E_{GABA} were considered for the meta-analysis. As there is a well described differential expression of KCC2 and NKCC1 at different stages of development, with KCC2 expression increasing and NKCC1 expression decreasing across development, only studies that used tissue older than postnatal day 7 were included (8 included data from younger animals). Other exclusion criteria included: reporting a significant change in NKCC1 (5 studies); use of non-rodent tissue (2 studies); no quantification of the change in KCC2 (2 studies). Nine experiments from eight

852 studies met all criteria and were included (Coull et al., 2003; Lagostena et al., 2010; Lee et al., 2011;
853 Ferrini et al., 2013; Campbell et al., 2015; MacKenzie and Maguire, 2015; Mahadevan et al., 2015;
854 Tang et al., 2015). However, one study did not report the change in V_m and hence was excluded from
855 the figure (Mahadevan et al., 2015). Data used in regression can be seen in Supplementary file 2 (Table
856 S2-1) and includes the analysis for regression against change in $[Cl^-]_i$. To accommodate varied
857 experimental preparations and techniques influencing data quality and biases, a 34-point scoring
858 system was designed to weight the studies (Table S2-2). A weighted least squares regression model
859 was then used to correlate the percentage (%) change in KCC2 expression versus change in Cl^- driving
860 force.
861

	Value	Description
Constants		
F	96485.33 C/mol	Faraday constant
R	8.31446 C/V	Universal gas constant
T	310.15 K	Absolute temperature (=37°C)
Parameters		
C_m	2×10^{-6} F/cm^2	Unit membrane capacitance (Qian and Sejnowski, 1989)
g_{Na}	20 µS/cm^2	Na^+ leak conductance (Kager et al., 2000)
g_K	70 µS/cm^2	K^+ leak conductance (Kager et al., 2000)
g_{Cl}	20 µS/cm^2	Cl^- leak conductance
g_{KCC2}	20 µS/cm^2	KCC2 conductance (Doyon et al., 2016)
v_w	0.018 dm^3/mol	Partial molar volume of water (Hernández and Cristina, 1998)
p_w	0.0015 dm/s	Osmotic permeability (Hernández and Cristina, 1998)
k_m	25 N/dm	Variable for membrane tension (higher than reported (Dai et al., 1998): used in this paper to accentuate differences in osmolarity)
p	0.1 C/(dm^2.s)	Default pump rate constant
$[Na^+]_o$	145 mM	Extracellular Na^+ concentration
$[K^+]_o$	3.5 mM	Extracellular K^+ concentration
$[Cl^-]_o$	119 mM	Extracellular Cl^- concentration

$[X^-]_o$	29.5 mM	Extracellular impermeant anion (X) concentration (Lodish et al., 2009; Raimondo et al., 2015)
D_{Na}	1.33×10^{-7} dm^2/s	Na^+ diffusion constant (Hille, 2001)
D_K	1.96×10^{-7} dm^2/s	K^+ diffusion constant (Hille, 2001)
D_{Cl}	2.03×10^{-7} dm^2/s	Cl^- diffusion constant (Hille, 2001)
Variables (default steady state)		
V_m	-72.6 mV	Membrane potential
$[Na^+]_i$	14.0 mM	Intracellular Na^+ concentration
$[K^+]_i$	122.9 mM	Intracellular K^+ concentration
$[Cl^-]_i$	5.2 mM	Intracellular Cl^- concentration
$[X^z]_i$	154.9 mM	Intracellular impermeant anion (X) concentration
z	-0.85	Average charge of intracellular X (Lodish et al., 2009; Raimondo et al., 2015)
w	2.0 pL (single compartment) 0.078 pL (multi-compartment)	Volume

Table 1: Constants, default parameters and usual steady state values for variables used in the biophysical models.

Slice preparation and electrophysiology. For all experiments, organotypic slices were prepared from rodent brain tissue. Wistar rats were used for the experiments testing the effects of CCC blockade. However, to allow for optogenetic manipulation, a crossed mouse strain on a C57BL/6 background was used. This mouse strain was a cross between mice expressing cre-recombinase in glutamic acid decarboxylase 2 (GAD2) positive interneurons (GAD2-IRES-cre, Jax Lab strain 010802) and mice with a loxP-flanked STOP cassette preventing transcription of the red-fluorescent protein tdTomato (a cre-reporter strain, Ai4, Jax Lab strain 007914.). This created the GAD2-cre-tdTomato strain which resulted in cre-recombinase and tdTomato expression in all GABAergic interneurons (Taniguchi et al., 2011). The use of all animals was approved by either the University of Oxford (rat) or the University of Cape Town (mouse) animal ethics committees.

877 Organotypic brain slices were prepared using 7 day old Wistar rats (CCC experiment) or crossed GAD2-
878 IRES-cre (Jax Lab strain 010802) and Ai14 tdtomato reporter (Jax Lab strain 007914) mice
879 (impermeant anion experiment) and followed the protocol originally described by (Stoppini et al.,
880 1991). Briefly, brains were extracted and swiftly placed in cold (4°C) dissection media consisting of
881 Gey's Balanced Salt Solution (GBSS #G9779, Sigma-Aldrich, USA) supplemented with D-glucose
882 (#G5767, Sigma-Aldrich, USA). The hemispheres were separated and individual hippocampi were
883 removed and immediately cut into 350 μm slices using a McIlwain tissue chopper (Mickle, UK). Cold
884 dissection media was used to rinse the slices before placing them onto Millicell-CM membranes
885 (#Z354988, Sigma-Aldrich, USA). Slices were maintained in culture medium consisting of 25% (vol/vol)
886 Earle's balanced salt solution (#E2888, Sigma-Aldrich, USA); 49% (vol/vol) minimum essential medium
887 (#M2279, Sigma-Aldrich, USA); 25% (vol/vol) heat-inactivated horse serum (#H1138, Sigma-Aldrich,
888 USA); 1% (vol/vol) B27 (#17504044, Invitrogen, Life Technologies, USA) and 6.2 g/l D-glucose. Slices
889 were incubated in a 5% carbon dioxide (CO2) humidified incubator at between 35 - 37°C. Recordings
890 were made after 6-14 days in culture. Previous studies have shown that after 7 days in culture
891 (equivalent to postnatal day 14) GABAergic signaling and E_{GABA} has sufficiently developed to a level
892 resembling mature nervous tissue (Streit et al., 1989; Wright et al., 2017). For the impermeant anion
893 experiment, the mouse organotypic brain slices were injected one day after culture with adeno-
894 associated vector serotype 1 (AAV1) containing a double-floxed sequence for channelrhodopsin
895 (ChR2) linked to a yellow fluorescent protein (YFP) tag driven by the elongation factor 1 promoter
896 (UNC Vector Core, USA). The vector was diffusely injected into slices using a custom-built Openspritzer
897 pressurized ejection device (Forman et al., 2017). Slices were left for 6 days in culture to allow for
898 robust expression of ChR2-YFP in GAD2+ interneurons.
899
900 For recordings, slices were transferred to a submerged chamber which was perfused with artificial
901 cerebro-spinal fluid (aCSF) bubbled with carbogen gas (95% oxgen:5% carbon dioxide). aCSF was
902 composed of (in mM): NaCl (120); KCl (3); MgCl2 (2); CaCl2 (2); NaH2PO4 (1.2); NaHCO3 (23); D-

903 Glucose (11) with pH adjusted to be between 7.35-7.40 using 0.1 mM NaOH. Neurons were visualized
904 using a 20X or 60x water-immersion objective (Olympus, Japan) on a BX51WI upright microscope
905 (Olympus, Japan). Widefield images were obtained using a Mightex CCE-B013-U CCD camera. For the
906 optogenetic experiments, we used epifluorescence microscopy to select slices that exhibited strong
907 ChR2-YFP expression throughout the hippocampal region. Micropipettes were prepared from
908 borosilicate glass capillaries with an outer diameter of 1.20mm and inner diameter of 0.69mm
909 (Warner Instruments, USA), using a horizontal puller (Sutter, USA). Recordings were made using
910 Axopatch 1D and Axopatch 200B amplifiers and acquired using pClamp9 (Molecular Devices) or
911 WinWCP software (University of Strathclyde, UK).
912
913 For the CCC blockade experiment gramicidin perforated patch recordings (Kyrozis and Reichling, 1995)
914 were performed using glass pipettes containing (in mM): 135 KCl, 4 Na_2ATP, 0.3 Na_3GTP, 2 $MgCl_2$, 10
915 HEPES and 80 µg/ml gramicidin (Calbiochem; pH 7.38; osmolarity, 290 mosmol/l). After obtaining a
916 cell-attached patch, the gramicidin perforation process was evaluated by continuously monitoring the
917 decrease in access resistance. Recordings were started once the access resistance had stabilized
918 between 20-80 MΩ, which usually occurred 20-40 min following gigaseal formation. Rupture of the
919 gramicidin patch, referred to as a break through, induces a large influx of the high Cl^- internal solution
920 into the cell. This causes a significant and permanent increase in the E_{GABA} at which time recordings
921 would be discarded. $GABA_AR$ activation was achieved by pressure application of muscimol (10 µM,
922 Tocris, UK), a selective $GABA_AR$ agonist, via a picrospritzer. To calculate $E_{GABA,}$ $GABA_AR$ currents were
923 elicited at different command voltages. These were a series of 10 mV steps above and below -60 mV.
924 Reported membrane potentials were corrected for the voltage drop across the series resistance for
925 each neuron. Holding current (reflecting membrane current) and total current (reflecting membrane
926 current plus the $GABA_AR$-evoked current) were plotted against the corrected holding potential to
927 generate a current-voltage (I-V) curve. Using this graph, the E_{GABA} was defined as the potential where
928 the total current equals the holding current. Some of the data used for calculating E_{GABA} values in

929 Figure 3E was also used in a previous study (Wright et al., 2017). V_m was defined as the x-intercept of
930 the holding current, and the driving force as the difference between the two. To block CCC function,
931 the KCC2 blocker furosemide (1mM, Sigma, USA) was applied.
932
933 For the impermeant anion experiments, whole-cell recordings were utilized as electroporation
934 consistently ruptured the gramicidin patches. Pipettes were filled with internal solution composed of
935 (in mM): Kgluconate (120); KCl (10); Na2ATP (4); NaGTP (0.3); Na2-phosphocreatinine (10) and HEPES
936 (10). To test the effect of introducing impermeant anions, we electroporated the anionic 10 000 MW
937 Dextran Alexa-Flour 488 (Thermo Fisher, USA) using a separate pipette positioned near the soma of
938 the patched cell. This molecule is a hydrophilic polysaccharide, which is both membrane impermeant
939 and highly negatively charged. Pipettes were filled with a 5% dextran solution in phosphate buffered
940 saline and voltage pulses (5-10 of 20 ms duration, 0.5-1 V) were applied using a stimulus isolator.
941 Successful electroporation of the anionic dextran was confirmed visually by observing the cell fill with
942 the fluorescent dye. Electroporation also resulted in immediate membrane depolarization, which
943 recovered over a period of 1-5 mins. $E_{GABA,}$ Vm and driving force were calculated during voltage steps
944 in voltage clamp mode (as above) with $GABA_A$Rs activated via endogenous synaptic release of GABA
945 using photo-activation of GAD2+ interneurons expressing ChR2-YFP with 100 ms pulses of blue light
946 using a 470 nm LED (Thorlabs), in the presence of 5 µM CGP-35348 (Torcis Bioscience, UK) to block
947 $GABA_B$R activation. $E_{GABA,}$ Vm and driving force were calculated before and atleast 5 mins following
948 electroporation to allow for stabilization of Vm, E_{GABA} and driving force. The image of the dextran filled
949 cell was acquired using a confocal microscope (LSM510 Meta NLO, Car Zeiss, Jena, Germany). Analysis
950 was performed using custom written scripts in the MATLAB environment (MathWorks). Numeric
951 results are presented as mean +/- SEM.

952 *References*

953

954 Ambros-Ingerson J, Holmes WR (2005) Analysis and comparison of morphological reconstructions of
955 hippocampal field CA1 pyramidal cells. Hippocampus 15:302–315.

956 Andrew RD, Labron MW, Boehnke SE, Carnduff L, Kirov SA (2007) Physiological evidence that
957 pyramidal neurons lack functional water channels. Cereb Cortex 17:787–802.

958 Armstrong CM (2003) The Na/K pump, Cl ion, and osmotic stabilization of cells. Proc Natl Acad Sci U S
959 A 100:6257–6262.

960 Baker PF, Willis JS (1972) Inhibition of the sodium pump in squid giant axons by cardiac glycosides:
961 dependence on extracellular ions and metabolism. J Physiol 224:463–475.

962 Ben-Ari Y (2002) Excitatory actions of GABA during development: the nature of the nurture. Nat Rev
963 Neurosci 3:728–739.

964 Berglund K, Wen L, Dunbar RL, Feng G, Augustine GJ (2016) Optogenetic Visualization of Presynaptic
965 Tonic Inhibition of Cerebellar Parallel Fibers. J Neurosci 36:5709–5723.

966 Burton RF (1983) The composition of animal cells: solutes contributing to osmotic pressure and charge
967 balance. Comp Biochem Physiol B 76:663–671.

968 Campbell SL, Robel S, Cuddapah V a., Robert S, Buckingham SC, Kahle KT, Sontheimer H (2015)
969 GABAergic disinhibition and impaired KCC2 cotransporter activity underlie tumor-associated
970 epilepsy. Glia 63:23–36.

971 Charron FM, Blanchard MG, Lapointe JY (2006) Intracellular hypertonicity is responsible for water flux
972 associated with Na+/glucose cotransport. Biophys J 90:3546–3554.

973 Coull JAM, Boudreau D, Bachand K, Prescott SA, Nault F, Sík A, De Koninck P, De Koninck Y (2003)
974 Trans-synaptic shift in anion gradient in spinal lamina I neurons as a mechanism of neuropathic
975 pain. Nature 424:938–942.

976 Dai J, Sheetz MP, Wan X, Morris CE (1998) Membrane Tension in Swelling and Shrinking Molluscan
977 Neurons. J Neurosci 18:6681–6692.

978 Diarra A, Sheldon C, Church J (2001) In situ calibration and [H+] sensitivity of the fluorescent Na+
979 indicator SBFI. Am J Physiol Cell Physiol 280:C1623–C1633.

980 Dierkes PW, Wüsten HJ, Klees G, Müller A, Hochstrate P (2006) Ionic mechanism of ouabain-induced
981 swelling of leech Retzius neurons. Pflugers Arch Eur J Physiol 452:25–35.

982 Dijkstra K, Hofmeijer J, van Gils S, van Putten MJAM (2016) A Biophysical Model for Cytotoxic Cell
983 Swelling. J Neurosci in press:11881–11890.

984 Doyon N, Prescott S a, Castonguay A, Godin AG, Kröger H, De Koninck Y (2011) Efficacy of synaptic
985 inhibition depends on multiple, dynamically interacting mechanisms implicated in chloride
986 homeostasis. PLoS Comput Biol 7:e1002149.

987 Doyon N, Vinay L, Prescott SA, De Koninck Y (2016) Chloride Regulation: A Dynamic Equilibrium Crucial
988 for Synaptic Inhibition. Neuron 89:1157–1172.

989 Farrant M, Kaila K (2007) The cellular, molecular and ionic basis of GABAA receptor signalling. Prog
990 Brain Res 160:59–87.

991 Ferrini F, Trang T, Mattioli TM, Laffray S, Del'Guidice T, Lorenzo L, Castonguay A, Doyon N, Zhang W,
992 Godin AG, Mohr D, Beggs S, Vandal K, Beaulieu J, Cahill CM, Salter MW, De Koninck Y (2013)
993 Morphine hyperalgesia gated through microglia-mediated disruption of neuronal Cl−
994 homeostasis. Nat Neurosci 16:183–192.

995 Fettiplace R, Haydon DA (1980) Water permeability of lipid membranes. Physiol Rev 60:510–550.

996 Földy C, Lee S-H, Morgan RJ, Soltesz I (2010) Regulation of fast-spiking basket cell synapses by the
997 chloride channel ClC-2. Nat Neurosci 13:1047–1049.

998 Forman CJ, Tomes H, Mbobo B, Burman RJ, Jacobs M, Baden T, Raimondo J V (2017) Openspritzer: an
999 open hardware pressure ejection system for reliably delivering picolitre volumes. Sci Rep 7:2188.

1000 Fraser JA, Huang CL-H (2004) A quantitative analysis of cell volume and resting potential determination
1001 and regulation in excitable cells. J Physiol 559:459–478.

1002 Gagnon MP, Bissonnette P, Deslandes LM, Wallendorff B, Lapointe JY (2004) Glucose Accumulation
1003 Can Account for the Initial Water Flux Triggered by Na+/Glucose Cotransport. Biophys J 86:125–
1004 133.

1005 Glykys J, Dzhala V, Egawa K, Balena T (2014) Local Impermeant Anions Establish the Neuronal Chloride
1006 Concentration. Science (80-):670–676.

1007 Hamada K, Matsuura H, Sanada M, Toyoda F, Omatsu-Kanbe M, Kashiwagi A, Yasuda H (2003)
1008 Properties of the Na^+/K^+ pump current in small neurons from adult rat dorsal root ganglia. Br J
1009 Pharmacol 138:1517–1527.

1010 Hernández J a, Cristina E (1998) Modeling cell volume regulation in nonexcitable cells: the roles of the
1011 Na+ pump and of cotransport systems. Am J Physiol - Cell Physiol 275:C1067–C1080.

1012 Hill T (1956) A. Fundamental studies. On the theory of the Donnan membrane equilibrium. Discuss
1013 Faraday Soc.

1014 Hille B (2001) Ion Channels of Excitable Membranes. Sunderl Massachusetts USA.

1015 Huberfeld G, Wittner L, Clemenceau S, Baulac M, Kaila K, Miles R, Rivera C (2007) Perturbed chloride
1016 homeostasis and GABAergic signaling in human temporal lobe epilepsy. J Neurosci 27:9866–
1017 9873.

1018 Hyde TM, Lipska BK, Ali T, Mathew S V, Law AJ, Metitiri OE, Straub RE, Ye T, Colantuoni C, Herman
1019 MM, Bigelow LB, Weinberger DR, Kleinman JE (2011) Expression of GABA signaling molecules
1020 KCC2, NKCC1, and GAD1 in cortical development and schizophrenia. J Neurosci 31:11088–11095.

1021 Jedlicka P, Deller T, Gutkin BS, Backus KH (2011) Activity-dependent intracellular chloride
1022 accumulation and diffusion controls GABA(A) receptor-mediated synaptic transmission.
1023 Hippocampus 21:885–898.

1024 Jiang C, Haddad GG (1991) Effect of anoxia on intracellular and extracellular potassium activity in
1025 hypoglossal neurons in vitro. J Neurophysiol 66:103–111.

1026 Kager H, Wadman WJ, Somjen GG (2000) Simulated seizures and spreading depression in a neuron
1027 model incorporating interstitial space and ion concentrations. J Neurophysiol 84:495–512.

1028 Kaila K, Price TJ, Payne J a., Puskarjov M, Voipio J (2014) Cation-chloride cotransporters in neuronal
1029 development, plasticity and disease. Nat Rev Neurosci 15:637–654.

1030 Kay AR (2017) How Cells Can Control Their Size by Pumping Ions. Front Cell Dev Biol 5:1–14.

1031 Keener J, Sneyd J (1998) Mathematical Physiology, Interdisciplinary Applied Mathematics 8.

1032 Klein PM, Lu A, Harper ME, McKown HM, Morgan J, Beenhakker MP (2017) Tenuous inhibitory
1033 GABAergic signaling in the reticular thalamus. J Neurosci:1345–17.

1034 Krishnan GP, Bazhenov M (2011) Ionic dynamics mediate spontaneous termination of seizures and
1035 postictal depression state. J Neurosci 31:8870–8882.

1036 Kuner T, Augustine GJ (2000) A Genetically Encoded Ratiometric Indicator for Chloride:: Capturing
1037 Chloride Transients in Cultured Hippocampal Neurons. Neuron 27:447–459.

1038 Kyrozis A, Reichling DB (1995) Perforated-patch recording with gramicidin avoids artifactual changes
1039 in intracellular chloride concentration. J Neurosci Meth 57:27–35.

1040 Lagostena L, Rosato-Siri M, D'Onofrio M, Brandi R, Arisi I, Capsoni S, Franzot J, Cattaneo A, Cherubini
1041 E (2010) In the Adult Hippocampus, Chronic Nerve Growth Factor Deprivation Shifts GABAergic
1042 Signaling from the Hyperpolarizing to the Depolarizing Direction. J Neurosci 30:885–893.

1043 Lee HHC, Deeb TZ, Walker JA, Davies PA, Moss SJ (2011) NMDA receptor activity downregulates KCC2
1044 resulting in depolarizing GABAA receptor–mediated currents. Nat Neurosci 14:736–743.

1045 Lewin N, Aksay E, Clancy CE (2012) Computational Modeling Reveals Dendritic Origins of GABA A -
1046 Mediated Excitation in CA1 Pyramidal Neurons. 7.

1047 Liang D, Bhatta S, Volodymyr G, Simard JM (2007) Cytotoxic edema : mechanisms of pathological cell
1048 swelling. Neurosurg Focus 22:1–9.

1049 Lodish H, Berk A, Zipursky SL, Matsudaira P, Baltimore D, Darnell J (2009) Intracellular Ion Environment
1050 and Membrane Electric Potential. In: Molecular Cell Biology, 4th ed. New York.

1051 MacAulay N, Gether U, Klærke DA, Zeuthen T (2002) Passive water and urea permeability of a human
1052 Na+-glutamate cotransporter expressed in Xenopus oocytes. J Physiol 542:817–828.

1053 MacKenzie G, Maguire J (2015) Chronic stress shifts the GABA reversal potential in the hippocampus
1054 and increases seizure susceptibility. Epilepsy Res 109:13–27.

1055 Mahadevan V, Dargaei Z, Ivakine EA, Hartmann A-M, Ng D, Chevrier J, Ormond J, Nothwang HG,
1056 McInnes RR, Woodin MA (2015) Neto2-null mice have impaired GABAergic inhibition and are
1057 susceptible to seizures. Front Cell Neurosci 9.

1058 Misgeld U, Deisz R a, Dodt HU, Lux HD (1986) The role of chloride transport in postsynaptic inhibition
1059 of hippocampal neurons. Science 232:1413–1415.

1060 Mohapatra N, Tønnesen J, Vlachos A, Kuner T, Deller T, Nägerl UV, Santamaria F, Jedlicka P (2016)
1061 Spines slow down dendritic chloride diffusion and affect short-term ionic plasticity of GABAergic
1062 inhibition. Sci Rep 6:23196.

1063 Nichol JA, Hutter F (1996) Tensile strength and dilatational elasticity of giant sarcolemmal vesicles
1064 shed from rabbit muscle. J Physiol 493:187–198.

1065 Price TJ, Cervero F, Gold MS, Hammond DL, Prescott SA (2009) Chloride regulation in the pain
1066 pathway. Brain Res Rev 60:149–170.

1067 Qian N, Sejnowski TJ (1989) An Electro-Diffusion Model for Computing Membrane Potentials and Ionic
1068 Concentrations in Branching Dendrites, Spines and Axons. Biol Cybern 62:1–15.

1069 Qian N, Sejnowski TJ (1990) When is an inhibitory synapse effective? Proc Natl Acad Sci USA 87:8145–
1070 8149.

1071 Raimondo J V., Burman RJ, Katz A a., Akerman CJ (2015) Ion dynamics during seizures. Front Cell
1072 Neurosci 9:1–14.

1073 Raimondo J V, Kay L, Ellender TJ, Akerman CJ (2012) Optogenetic silencing strategies differ in their
1074 effects on inhibitory synaptic transmission. Nat Neurosci 15:1102–1104.

1075 Raimondo J V, Richards BA, Woodin MA (2017) Neuronal chloride and excitability — the big impact of
1076 small changes. Curr Opin Neurobiol 43:35–42.

1077 Rivera C, Voipio J, Thomas-Crusells J, Li H, Emri Z, Sipilä S, Payne JA, Minichiello L, Saarma M, Kaila K
1078 (2004) Mechanism of activity-dependent downregulation of the neuron-specific K-Cl
1079 cotransporter KCC2. J Neurosci 24:4683–4691.

1080 Rungta RL, Choi HB, Tyson JR, Malik A, Dissing-Olesen L, Lin PJC, Cain SM, Cullis PR, Snutch TP, Macvicar

1081 BA (2015) The cellular mechanisms of neuronal swelling underlying cytotoxic edema. Cell
1082 161:610–621.

1083 Sachs F, Sivaselvan M V. (2015) Cell volume control in three dimensions: Water movement without
1084 solute movement. J Gen Physiol 145:373–380.

1085 Savtchenko LP, Poo MM, Rusakov DA (2017) Electrodiffusion phenomena in neuroscience: a neglected
1086 companion. Nat Publ Gr 18:598–612.

1087 Sperelakis N (2012) Chapter 10 – Gibbs–Donnan Equilibrium Potentials. In: Cell Physiology Source
1088 Book, pp 147–151.

1089 Staley KJ, Proctor WR (1999) Modulation of mammalian dendritic GABAA receptor function by the
1090 kinetics of Cl- and HCO3- transport. J Physiol 519:693.

1091 Stoppini L, Buchs PA, Muller D (1991) A simple method for organotypic cultures of nervous tissue. J
1092 Neurosci Methods 37:173–182.

1093 Streit P, Thompson SM, Gahwiler BH (1989) Anatomical and Physiological Properties of GABAergic
1094 Neurotransmission in Organotypic Slice Cultures of Rat Hippocampus. Eur J Neurosci 1:603–615.

1095 Tang D, Qian A, Song D, Ben Q, Yao W, Sun J, Li W, Xu T, Yuan Y (2015) Role of the potassium chloride
1096 cotransporter isoform 2-mediated spinal chloride homeostasis in a rat model of visceral
1097 hypersensitivity. Am J Physiol Gastrointest Liver Physiol 308:G767-78.

1098 Taniguchi H, He M, Wu P, Kim S, Paik R, Sugino K, Kvitsiani D, Kvitsani D, Fu Y, Lu J, Lin Y, Miyoshi G,
1099 Shima Y, Fishell G, Nelson SB, Huang ZJ (2011) A resource of Cre driver lines for genetic targeting
1100 of GABAergic neurons in cerebral cortex. Neuron 71:995–1013.

1101 Thompson SM, Gähwiler BH (1989) Activity-dependent disinhibition. II. Effects of extracellular
1102 potassium, furosemide, and membrane potential on ECl- in hippocampal CA3 neurons. J
1103 Neurophysiol 61:512–523.

1104 Tosteson DC, Hoffman JF (1960) Regulation of cell volume by active cation transport in high and low
1105 potassium sheep red cells. J Gen Physiol 44:169–194.

1106 Tyzio R, Minlebaev M, Rheims S, Ivanov A, Jorquera I, Holmes GL, Zilberter Y, Ben-Ari Y, Khazipov R
1107 (2008) Postnatal changes in somatic gamma-aminobutyric acid signalling in the rat hippocampus.
1108 Eur J Neurosci 27:2515–2528.

1109 Tyzio R, Nardou R, Ferrari DC, Tsintsadze T, Shahrokhi A, Eftekhari S, Khalilov I, Tsintsadze V,
1110 Brouchoud C, Chazal G, Lemonnier E, Lozovaya N, Burnashev N, Ben-Ari Y (2014) Oxytocin-
1111 mediated GABA inhibition during delivery attenuates autism pathogenesis in rodent offspring.
1112 Science (80-) 343:675–679.

1113 Voipio J, Boron WF, Jones SW, Hopfer U, Payne J a, Kaila K (2014) Comment on “Local impermeant
1114 anions establish the neuronal chloride concentration”. Science 345:1130.

1115 Wright R, Newey SE, Ilie A, Wefelmeyer W, Raimondo J V., Ginham R, Jeffrey Mcllhinney RA, Akerman
1116 CJ (2017) Neuronal chloride regulation via KCC2 is modulated through a GABAB receptor protein
1117 complex. J Neurosci 37:5447–5462.

1118 Xiao A, Wei L, Xia S, Rothman S, Yu S (2002) Ionic mechanisms of ouabain-induced concurrent
1119 apoptosis and necrosis in individual cultured cortical neurons. J Neurosci 15:4.

1120 Yeh BK, Lazzara R (1973) Reversal of Ouabain-Induced Electrophysiological Effects by Potassium
1121 Canrenoate in Canine Purkinje Fibers. Circ Res 32:501–508.

1122 Zeuthen T (1994) Cotransport of K+, Cl- and H2O by membrane proteins from choroid plexus
1123 epithelium of Necturus maculosus. J Physiol 478 (Pt 2:203–219.